

Development of differential absorption spectroscopy techniques for a sub-millimeter wave radar system

Master's thesis in Wireless, photonics and space engineering

Sebastian Göbel

MASTER'S THESIS 2021

**Development of differential absorption spectroscopy
techniques for a sub-millimeter wave radar system**

Sebastian Göbel



CHALMERS
UNIVERSITY OF TECHNOLOGY

Department of microtechnology and nanoscience
Terahertz and Millimetre Wave Laboratory
CHALMERS UNIVERSITY OF TECHNOLOGY
Gothenburg, Sweden 2021

Synthesis and evaluation of differential absorption spectroscopy retrieval methods
Sebastian Göbel

© Sebastian Göbel, 2021.

Supervisors: Tomas Bryllert, Department of microtechnology and nanoscience, Marlene
Bonmann, Department of microtechnology and nanoscience
Examiner: Jan Stake, Department of microtechnology and nanoscience

Master's Thesis 2021
Department of microtechnology and nanoscience
Terahertz and Millimetre Wave Laboratory
Chalmers University of Technology
SE-412 96 Gothenburg
Telephone +46 31 772 1000

The absorption cross section for water vapor at atmospheric conditions

Typeset in L^AT_EX
Printed by Chalmers Reproservice
Gothenburg, Sweden 2021

Synthesis and evaluation of differential absorption spectroscopy retrieval methods
Sebastian Göbel
Department of microtechnology and nanoscience
Chalmers University of Technology

Abstract

To reduce the negative impact of the increasing energy demands of society onto the climate, the use of renewable resources is essential. In this context, power plants for combustion of sustainable biomass fuels play an important role. For an efficient combustion process to take place, mixing of the fluid solids, the gas-solid contacts, and heat transfer are of importance, and fluidized bed technology is used for large-scale combustion and gasification of solid fuels. For further optimization of combustion, the mixing processes of fluidized beds are under investigation using experiments and theoretical modelling. However, theoretical methods are often hard to validate with appropriate experimental results, and the experimental methods often lack the desired resolution in time and space. In contrast, a sub-millimeter wave radar may be a suitable tool to resolve particle concentrations and velocities. Furthermore, the existence of water absorption lines within the radars frequency range can facilitate even water vapor content extraction.

In this thesis, a retrieval method inspired by NASA's Vapor In-Cloud Profiling Radar (VIPR) project is synthesized and evaluated using simulations to achieve a sense of expectations, and experimentally in a lab environment using falling particles to mimic the fluidized bed. Further, a fixed target method is evaluated which could prove helpful in measuring water vapor. Experimentally, the initial tests show promising performance of range resolved measurements of particle concentration, suggesting further evaluation is of interest.

Keywords: radar, retrieval, water, vapor, differential, absorption, spectroscopy.

Acknowledgements

I would like to extend my gratitude to my supervisors Tomas Bryllert and Marlene Bonmann for their guidance and help carrying out experiments during this thesis. I would further like to extend my gratitude to Mats Myremark for the advice and aid with the mechanical construction of the test chamber used for experiments. Lastly I would like to extend my gratitude to my examiner Jan Stake for offering me this opportunity which led to me learning more about more subjects than I could have expected.

Sebastian Göbel, Gothenburg, October 2021

Contents

List of Figures	xi
List of Tables	xiii
1 Introduction	1
1.1 The process reactor and its environment	1
1.2 Differential absorption spectroscopy	1
1.3 Previous work in differential absorption spectroscopy	2
2 Theory	3
2.1 Radar essentials	3
2.1.1 FMCW Radar	4
2.1.2 Radar equation	6
2.1.3 Swerling targets	6
2.1.4 Range-Doppler processing	6
2.1.5 Frequency resolved FMCW radar	6
2.1.6 Coherent integration	7
2.1.7 In-coherent integration	7
2.2 Scattering and absorption by particles	7
2.2.1 Backscatter cross section	8
2.2.2 Extinction cross section	9
2.2.3 Mie theory - single spherical particle	9
2.3 Absorption spectroscopy	10
2.3.1 Radiative transfer / Beer-Lamberts law	10
2.3.2 Attenuation in a gas	11
2.3.3 Line by line approach	11
3 Experimental setups	15
3.1 Radar configuration	15
3.2 Experimentation with fixed targets	15
3.3 Experimentation with falling particles	17
4 Retrieval methods	19
4.1 Water vapor retrieval from fixed target	19
4.2 Water vapor retrieval in particulate medium	20
4.2.1 Assumptions and conditions	20
4.2.2 Radar processing	21

4.2.3	Retrieval method	22
4.3	Simulation of expected performance of retrieval method	27
5	Results	29
5.1	Experimentation with fixed target	29
5.2	Experimentation with falling particles	33
5.3	Simulation of expected performance in a particulate medium	36
6	Conclusion	39
6.1	Fixed target experiments	39
6.2	Retrieval method: Formulation, experiments and simulations	39
6.3	Future work	40
6.3.1	Particles	40
6.3.2	Water vapor concentration	40
6.3.3	Reference measurements	40
6.3.4	Experimental setup	40
6.3.5	Retrieval method	41
6.3.6	Integration method	41
A	Appendices	I
A.1	Noise model for retrieval method	I
A.2	Code used for simulations	III

List of Figures

2.1	The saw-tooth frequency chirp profile of an FMCW radar, both with a transmitted signal and a delayed reflected signal. Marked are the key parameters such as round-trip delay τ , pulse length T_p , bandwidth BW and the frequency difference ΔF in transmitted and received signals.	4
2.2	The IF signal of three targets at different ranges, shown on logarithmic y-axis scale. The signal is shown both with a rectangular and Hamming window, it is seen that using a Hamming window heavily reduces the spread of a target in range.	5
2.3	Backscatter efficiency $\frac{\sigma_b}{\pi r^2}$ of a sphere of perfect electrical conductor as a function of its relative size. The three regions are clearly visible: Rayleigh, Mie(resonance) and geometrical, the Rayleigh and geometrical dependency is marked with an asymptotic line. It is worth noting that even at larger relative sizes the oscillating behavior remains but quickly becomes smaller.	8
2.4	The absorption cross section of water vapor under normal atmospheric conditions ($P = 1 \text{ atm}$, $T = 290 \text{ K}$), in $\text{dBg}^{-1}\text{m}^3\text{km}^{-1}$, the inset shows the bandwidth of the radar used in this thesis.	11
3.1	A simplified block diagram for the radar used in the experiments.	15
3.2	The experimental setup used for fixed target measurements. The chamber allows for controlling the water vapor concentration in the path of the beam.	16
3.3	Test setup for falling particles	17
4.1	The absorption cross section of water vapor under normal atmospheric conditions ($P = 1 \text{ atm}$, $T = 290 \text{ K}$), in $\text{dBg}^{-1}\text{m}^3\text{km}^{-1}$, the zoomed-in section is for the bandwidth of the radar used in this thesis. The attenuation is varying and steadily increasing with absorption peaks at certain frequencies.	19
4.2	The block diagram of an equivalent signal processing chain to the one used, simplified to omit unrelated parts of the chain. Fast time index is t , slow time is T and distance to target monitored is r_T	20
4.3	The block diagram of an equivalent signal processing chain to the one used, simplified to highlight the main steps. Fast time index is t , frequency is f and slow time is T . All steps are done independently for each sub-band.	21

5.1	A time series comparison between the radar high/low frequency ratio, R and the hygrometer's water vapor concentration reading. It can be observed that there is a strong correlation between the humidity reading and the radar reading, although drift is also noticeable.	30
5.2	A scatter plot comparison between the radar high/low ratio and the hygrometer's water vapor concentration reading, a clear linear relation is observed with a measured slope displayed in the legend of the figure. The drift over time seen in Figure 5.1 can be seen as there appears to be two different lines merging into one.	31
5.3	The full range span measurement of the time-averaged water vapor ρ and particle concentration n , the data is shown with error bars marking the 1σ uncertainty. The readings are somewhat constant with the exception of an out-liar at range index 13.	33
5.4	The optimal range span measurement of the time-averaged water vapor ρ and particle concentration n , the data is shown with 1σ uncertainty as error bars. The readings are more consistent compared to the full span.	34
5.5	A comparison between the true and retrieved particle and water vapor concentration profiles, this with an integration time of 1 sec. For this short of an integration time both particle and water vapor concentration is very uncertain. The SNR is also shown over range for all the different frequencies.	36
5.6	A comparison between the true and retrieved particle and water vapor concentration profiles, this with an integration time of 10 sec. At this long of an integration time the particle concentration is becoming increasingly accurate while the humidity is still not good enough for room temperature humidity, but could be useful at much higher concentrations. The SNR is also shown over range for all the different frequencies.	37
5.7	A comparison between the true and retrieved particle and water vapor concentration profiles, this with an integration time of 100sec. At this integration time the particle measurements are becoming accurate and the humidity measurements are still not enough for room humidity but can be comparable to that needed in a process reactor. The SNR is also shown over range for all the different frequencies.	38

List of Tables

4.1	The different parameters used for the measurements shown in section 5.2. Where f_0 is center frequency, BW the total bandwidth, N_f the number of frequency points, D diameter of particles in model, ϵ_r relative permittivity of particles in model, P the ambient pressure, T the ambient temperature and $\frac{N_{ind}}{T_{int}}$ the number of statistically independent measurements per second of integration.	22
4.2	The different parameters used for the simulations shown in section 5.3. Which include the center frequency of the radar f_0 , the total bandwidth of the radar BW , the number of frequency points N_f , the diameter of the particles measured D , the dielectric permittivity of the particles ϵ_r , the ambient pressure P , the ambient temperature T and the number of statistically independent samples per second of integration $\frac{N_{ind}}{T_{int}}$	27
5.1	The factors used to estimate the total mass fallen during the experiment m_{tot} using the length of the experiment T_{exp} , estimated time average particle density \hat{n}	35

1

Introduction

The driving force behind this thesis is the desire to monitor the humidity and particle concentration inside a power reactor for biomass combustion at the Chalmers power plant [1]. The goal being a measurement of the three dimensional distribution of water vapor which would allow one to visualize hot spots, although for this thesis the scope is limited to one dimension. These hot spots could indicate that the stirring method used is insufficient, this being placing the wood fuel on a fluidized bed of sand. This could mean a drop in efficiency and thus having access to this diagnostic tool could allow one to optimize the stirring of fuel and there by increase the efficiency of the power reactor. This being useful in improving the performance of a renewable source of energy and thus important for a future with renewable sources of energy.

This report investigates the opportunity of using a sub-millimeter wave radar for water vapor retrievals inside of a power reactor, both theoretically and in a limited form experimentally. The theoretical result is a proposal of a retrieval method, with idealized estimates of its expected performance. The experimental results are limited testing of the retrieval method and of in-lab tests of an alternative mode of operation, where the humidity is monitored without the particulate environment of the power reactor.

1.1 The process reactor and its environment

The process reactor is a chamber containing a fluidized bed of sand where fuel in the form of wood chips is burnt, the fluidized bed allows for the dispersal of the fuel in the chamber. The burnt fuel generates water vapor which is the output of the reactor, thus it is of interest to monitor the distribution of the water vapor concentration inside the chamber.

The inside of the reactor is extremely warm (several hundreds of degrees Celsius) and contains different gases, notably water vapor in great amounts (order of a hundred gram per cubic meter) which makes it difficult to monitor the reactions in the power reactor by technologies that require direct contact with the gases etc in the reactor.

1.2 Differential absorption spectroscopy

A method for remotely monitoring the inside of the chamber is differential absorption spectroscopy. As electromagnetic radiation propagates an environment it loses energy by absorption by the gases in the environment. This allows one to estimate the concentration of an absorbing gas species. In *Differential* absorption spectroscopy the frequency

dependent contrast of the absorption is used to estimate the concentration rather than as an example relying on comparing the power before and after the gas environment. This allows the method to be used in situations where calibrating the system by removing the absorbing gas species and comparing the measurements with and without the gas [2].

1.3 Previous work in differential absorption spectroscopy

Range resolved differential absorption spectroscopy has been used at optical frequencies, notably in Differential Absorption spectroscopy Lidar, DIAL [2]. Recently it has been used by NASA at millimeter wave frequencies. Notably in NASA's work on humidity measurements inside clouds [3]–[7], the work of which served as an excellent inspiration for this thesis. The problem of measuring humidity inside clouds is quite similar to the problem posed by measuring humidity inside the fluidized bed of a process reactor. Instead of a cloud of water droplets there is a cloud of small sand particles, the differences lie in the geometry and amount of water vapor. A cloud is much larger, thus less range resolution is needed while the water vapor concentration in a process chamber is much higher than a cloud thus less humidity resolution is needed.

2

Theory

This chapter covers the theory needed to understand this report. It starts with radar essentials, such as different methods of integration and more advanced processing such as range Doppler processing to allow distance and velocity measurements, later used to remove stationary targets in section 4.2. Continuing with how scattering and absorption of particles is described and characterized, and how these characteristics are calculated. Finishing with describing how electromagnetic waves can be absorbed by gases and how this is modelled, showing how to calculate the absorption behavior. The latter two are later used in section 4.2 to build a model of the interaction between the radar beam and the particles and gas inside the experiment.

2.1 Radar essentials

This section describes a few essentials for radar, focusing specifically on frequency modulated continuous wave (FMCW) radar, as it is the radar used in this thesis. In general a radar works by transmitting an electromagnetic wave and comparing the time difference between it and the reflected echo from a target, this to determine the distance or range to the target [8, ch. 1].

2.1.1 FMCW Radar

An FMCW radar transmits a wave which in theory has a constant amplitude but a repeating frequency modulation such as a saw-tooth [8, ch. 8]. Which is used in this report, where the instantaneous frequency transmitted is linearly increased and then quickly lowered only to be repeated again, this can be seen in Figure 2.1. The length of each sweep is referred as the pulse length, or sometimes sweep time: T_p in the case of FMCW radar. Its inverse being the pulse repetition frequency: PRF , assuming no waiting period in-between the pulses. The difference between the maximum and minimum frequency is the bandwidth: BW , while the center frequency: f_0 lies between the two.

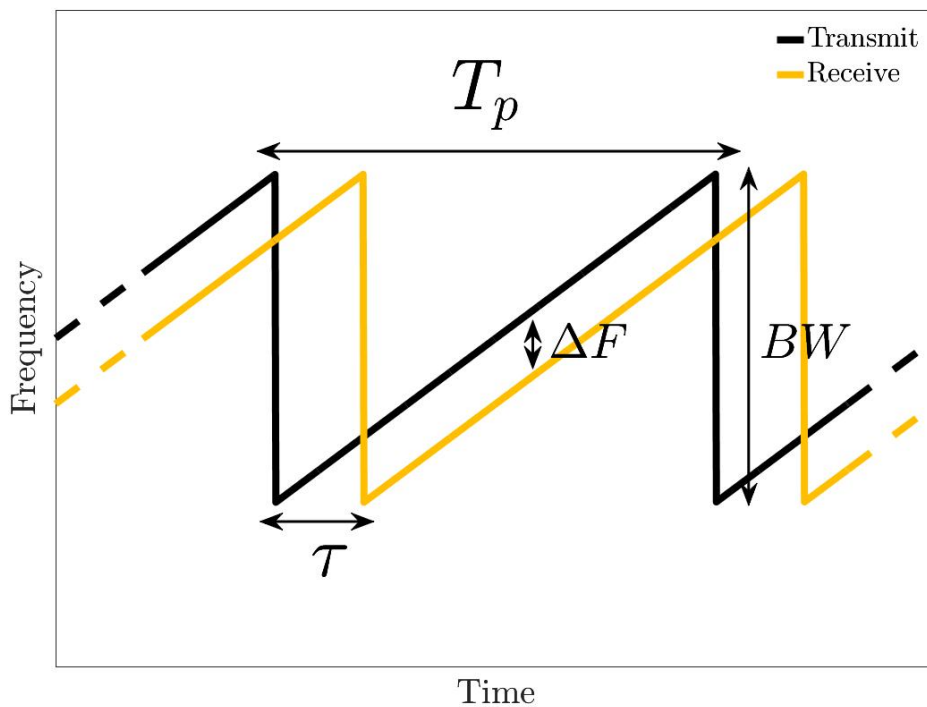


Figure 2.1: The saw-tooth frequency chirp profile of an FMCW radar, both with a transmitted signal and a delayed reflected signal. Marked are the key parameters such as round-trip delay τ , pulse length T_p , bandwidth BW and the frequency difference ΔF in transmitted and received signals.

The received pulse from a point target will be delayed compared to the transmitted, with a different amplitude and phase. This means that the frequency modulation is maintained but shifted in time. For the modulation that's used (sawtooth) this means that the frequency difference between the transmitted and received wave is constant and proportional to the delay, and thus also range.

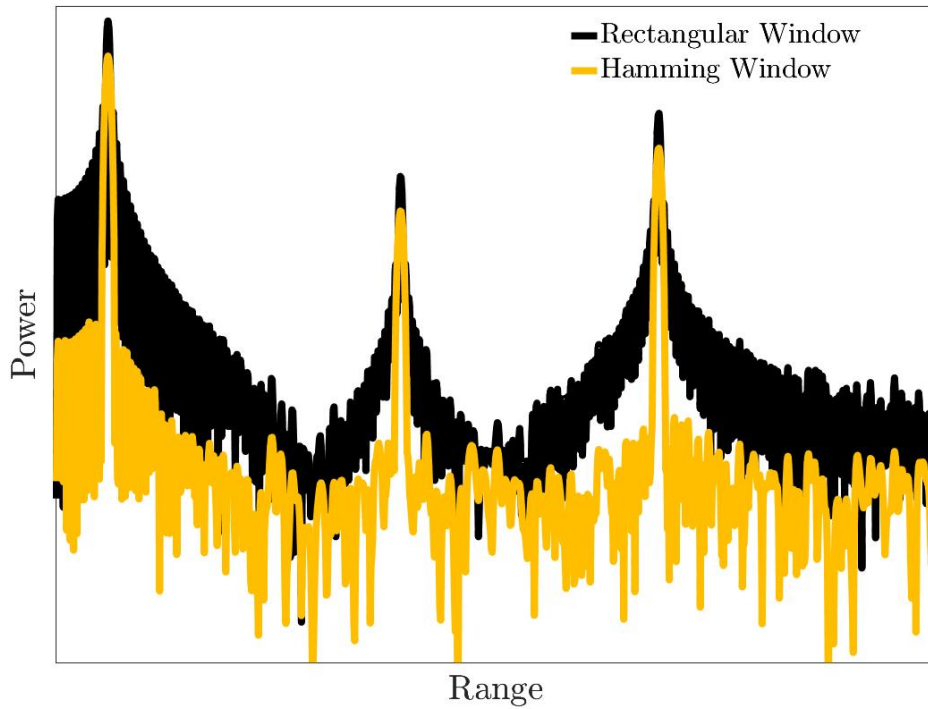


Figure 2.2: The IF signal of three targets at different ranges, shown on logarithmic y-axis scale. The signal is shown both with a rectangular and Hamming window, it is seen that using a Hamming window heavily reduces the spread of a target in range.

The received signal of the radar is mixed with the transmitted to obtain the difference frequency, called an intermediate frequency (IF). The IF is then sampled using an analog to digital converter for further digital processing. In order to obtain the range information from the IF signal, the sampled signal is then Fourier transformed to produce a range profile, an example of which can be seen in Figure 2.2.

The delay between the outgoing and incoming wave $\tau = \frac{2R}{C_0}$ is the round trip delay to and from the target at distance R at the speed of light C_0 . The instantaneous frequency $f_{TX}(t) = f_0 + \frac{BW}{2T_p}(t - T_p)$, combining these two equations yields an equation for the IF frequency $f_{IF}(r)$ as a function of range, which can be seen in Equation 2.1.

$$f_{IF}(r) = \frac{2BW}{T_p C_0} R \quad (2.1)$$

When multiple pulses are being processed the time scale of a chirp (which is Fourier transformed to obtain a range profile) the time is referred to "fast time", while the time scale for several pulses (to study how the range profile changes over time) is referred to as "slow time".

2.1.2 Radar equation

The radar equation 2.2 describes the received power P_r using the antenna gain G , free space wavelength λ , one way distance R , transmitted power P_t and the radar cross section σ [8, Ch. 1]. The radar cross section which describes the amount of intensity that is reflected back towards the source by an object and will instead be referred to as the back-scatter cross section σ_b , to differentiate it from other cross sections.

$$P_r = P_t \frac{G^2 \sigma \lambda^2}{(4\pi)^3 R^4} \quad (2.2)$$

2.1.3 Swerling targets

As seen in subsection 2.1.2, the received power is dependent on the targets back-scatter cross section. In certain cases the back-scatter cross section is not constant between each sweep/pulse, which could for example be caused by interference between several reflections. Swerling targets describe the different scenarios and their statistics, for this thesis Swerling targets of type Swerling-2 are of interest as it is applicable for the intended use case of a cloud of particles. These are caused by many scattering objects each with a similar back-scatter cross-section interfering with each other, causing the received power to be random and following an exponential distribution [9]. The expected back-scatter cross-section and its variance is equal as seen in Equation 2.3 [9].

$$E[\sigma_b] = \sqrt{\text{VAR}[\sigma_b]} \quad (2.3)$$

2.1.4 Range-Doppler processing

Using the Doppler shift from a reflection the velocity of a target can be estimated, however only toward/against the radar ($\vec{v} \cdot \vec{r}$). This can be combined with range detection for Range-Doppler processing, where one can see the intensity of targets at a certain range and velocity [8, ch. 4]. This is done in practice by collecting several range profiles over time and doing a Fourier transform for each range. This is later used in section 4.2 to remove reflections from stationary targets and only keep those from moving particles.

2.1.5 Frequency resolved FMCW radar

In certain applications such as differential absorption spectroscopy it is interesting to do radar measurements at several frequencies. Which can be used to accurately solve for certain physical parameters of the target scene, such as water vapor concentration or other frequency dependent behavior [6]. This can be done by shifting the local oscillator of the radar [4] or by using several radar systems. In this report a different approach will be used. Instead the wide bandwidth of the radar will be utilized and the chirp will be divided in fast time into several snippets where each one corresponds to a certain frequency band. Having radar measurements for different frequencies lays the foundation behind the differential absorption spectroscopy approach, since it relies on estimating the concentration of for example a gas using the frequency dependent attenuation through the medium, as

seen in section 4.2.

$$\Delta R \Delta f = \frac{C_0}{2} \quad (2.4)$$

Each of these sub-bands now have a bandwidth of $\Delta f = \frac{BW}{N_f}$ and thus the radar will have a frequency resolution of Δf , where BW is the total bandwidth and N_f the number of frequency points, then re-write the range resolution formula [8, ch. 8] and include the frequency resolution. This equation is shown in Equation 2.4. This means that there is a trade-off in-between range and frequency resolution, thus one needs to sacrifice range resolution in order to do spectroscopic measurements using a radar.

2.1.6 Coherent integration

Coherent integration of wave-forms is done by adding the IF waveform in the time or frequency domain of the signals for several pulses [10]. This will only work for signals where the signal retains its phase over the many samples, it is then said to be coherent [8, ch. 1]. This is used in section 4.1 to improve the signal to noise ratio, and thus stabilize the measurement.

2.1.7 In-coherent integration

If the reflection from a target is not coherent such as in the case of multiple reflectors who's reflections interfere with each other as they move around in a random manner. Instead of integrating the complex amplitude, the power (absolute squared amplitude) is integrated [10]. This is used to estimate the average received power from a Swerling target in subsection 4.2.2.

2.2 Scattering and absorption by particles

This section describes how electromagnetic waves interact with particles in a medium, such as small dielectric spheres in air. It starts by describing first in general how the behavior is treated and then introduces Mie-theory which is an analytical solution to scattering and absorption by spheres of any size. The contents of this section is important for the retrieval method in section 4.2, which relies on the later discussed extinction cross section to estimate the range dependent concentration of particles in the path of the beam.

Light propagating through a medium containing particles of a contrasting refractive index will scatter and be absorbed. The scattering will both send light back towards the source and reduce the forward going wave by scattering it in other directions [11, ch. 1]. The absorption by the particles will convert a part of the energy to heat, thus also reducing the strength of the forward going wave [11, ch. 1]. The strength of the absorption and scattering is characterized by different cross sections, which are in general dependent on the shape, orientation, the refractive index of the particle and the surrounding medium

and frequency [11, ch. 1].

In general small particles scatter in a way referred to as Rayleigh scattering, where the behavior as a function of the size parameter $\frac{r}{\lambda}$ is similar [11, ch. 5]. For larger particles the cross section starts being describable using geometrical optics, in-between these two regions lie the Mie Region or resonance region where the behavior of the particle is highly dependent on the size parameter [11, ch. 6].

2.2.1 Backscatter cross section

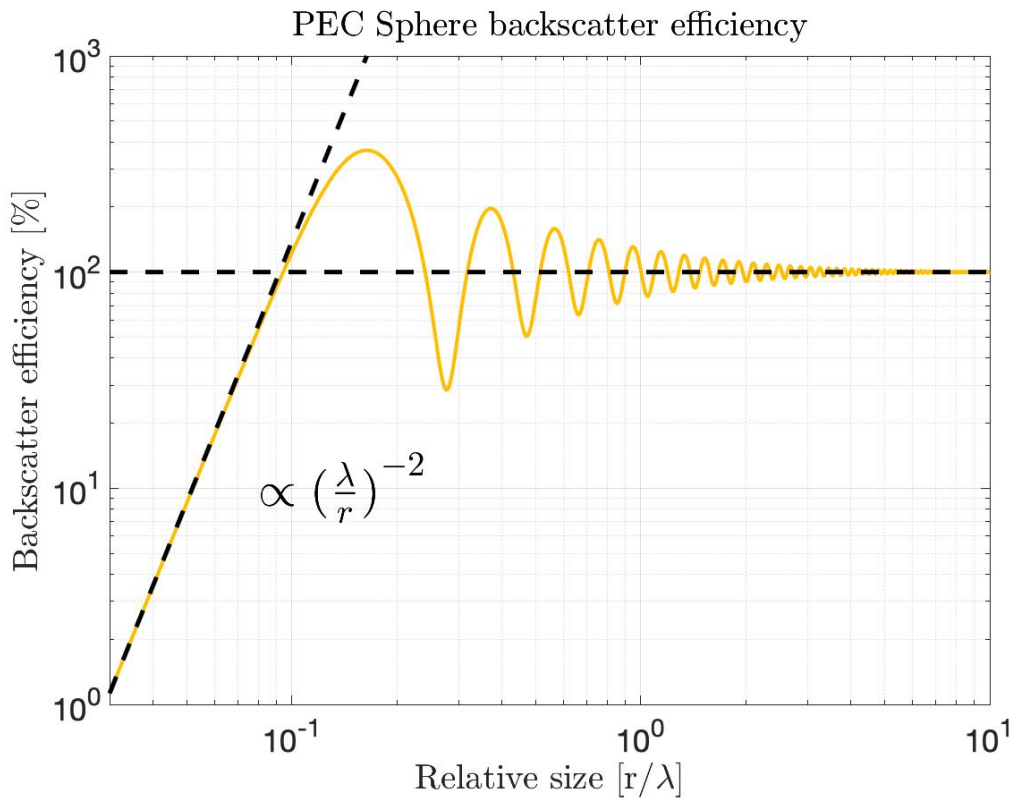


Figure 2.3: Backscatter efficiency $\frac{\sigma_b}{\pi r^2}$ of a sphere of perfect electrical conductor as a function of its relative size. The three regions are clearly visible: Rayleigh, Mie(resonance) and geometrical, the Rayleigh and geometrical dependency is marked with an asymptotic line. It is worth noting that even at larger relative sizes the oscillating behavior remains but quickly becomes smaller.

The back-scatter cross section σ_b (also referred to as the mono static radar cross section [8, ch. 1]) describes the amount of electromagnetic energy that is scattered back towards the direction of which it came [11, ch. 4], used in the radar equation in subsection 2.1.2. It is possible to interpret the size of the cross-section as the geometrical cross section of a perfectly electrical conducting sphere that would scatter the same amount of energy as a the object in question, and thus allows one to describe the cross section of spheres as an efficiency times the geometrical cross section as seen in Equation 2.5 [11, ch. 4].

The backscatter efficiency for a perfectly conducting sphere is shown as a function of size relative to wavelength in Figure 2.3.

$$\sigma_b = \sigma_b \cdot \pi r^2 \quad (2.5)$$

2.2.2 Extinction cross section

The extinction cross-section describes the reduction in forward going intensity by both absorption and scattering, as both contribute to the reduction in intensity [11, ch. 3]. For spherical particles it can also be described using an efficiency Q times the geometrical cross section of a sphere πr^2 , as seen in Equation 2.6 [11, ch. 4]. The extinction cross section σ_{ext} is added into Beer-Lamberts law as seen in Equation 2.7, where $I(z)$ is the intensity, I_0 is the initial intensity, n the particle concentration and z is the distance into the absorbing medium [11, ch. 3].

$$\sigma_{ext} = \sigma_{sca} + \sigma_{abs} = (Q_{sca} + Q_{abs}) \cdot \pi r^2 \quad (2.6)$$

$$I(z) = I_0 \cdot \exp(-\sigma_{ext} \cdot n \cdot z) \quad (2.7)$$

2.2.3 Mie theory - single spherical particle

Mie theory is the analytical solution of the interaction in-between an electromagnetic plane wave and a sphere of refractive index m_1 in an environment with refractive index m_2 , while strictly correct for spherical particles it offers a first order approximation for all roughly spherical particles [11, p. 4]. The derivation and physics of Mie theory are somewhat outside the scope of this thesis, since the details of Mie theory are not used it is sufficient to know that the cross sections used originate from Mie theory. For solving the Mie theory of particles a Matlab script [12] was used, which outputs the different cross sections.

2.3 Absorption spectroscopy

When electromagnetic radiation propagates in a gas it can excite the different molecular resonances of the molecules in the gas, causing them to absorb part of the wave's energy and thus reducing its intensity [2, Ch. 4]. This chapter describes how this is modelled and calculated, this to provide the reader with information about the dependency of the environment (temperature, pressure, etc). As different gases have transitions at different frequencies it allows one to independently measure their concentrations, which is useful in applications such as atmospheric measurements using lasers [2, Ch. 5]. The content of this section will be used in section 4.2 to estimate the range dependent concentration of water vapor, as well describes the main phenomenon seen in section 4.1. It further also shows the temperature, pressure dependencies for the parameters that describe the attenuation spectrum, which is important in deciding which kind of environment the retrieval method proposed in section 4.2 may work in.

2.3.1 Radiative transfer / Beer-Lamberts law

When a plane-wave travels through a non radiating homogeneous medium but absorbing and scattering medium the forward going beam intensity $I(\vec{r})$ is described by Beer-Lamberts law seen in Equation 2.8, where the beam is directed in the \hat{r} direction and $I(\vec{r})$ is the intensity at \vec{r} [11, Ch. 3]. Here α is the total extinction of the medium, which can originate from absorption or scattering making the energy change direction and thus effectively be reduced [2, Ch. 1]. For mediums such as a gas mixture with containing particles the extinction will be the sum of gas absorption (see section 2.3) and extinction by the particles (see section 2.2).

$$\ln\left(\frac{I(\vec{r}_1)}{I(\vec{r}_2)}\right) = \int_{r_1}^{r_2} \alpha(r) \cdot dr \quad (2.8)$$

2.3.2 Attenuation in a gas

As previously mentioned in subsection 2.3.1 the intensity of a \hat{z} traveling plane wave in an attenuating medium can be described using Beer-Lambert's law which is shown in Equation 2.9, with α being the extinction coefficient usually in dB/km or simply in natural units $1/m$. In this chapter it is shown how to calculate the extinction from gas absorption using a line by line approach and data from HITRAN[13], an approach that works all the way from low frequency radio to ultra-violet and in-between. The results of this section are used to calculate the absorption cross section of water vapor in atmospheric conditions, as shown in Figure 2.4.

$$I(z) = I_0 \cdot \exp(-\alpha(\nu) \cdot z) \quad (2.9)$$

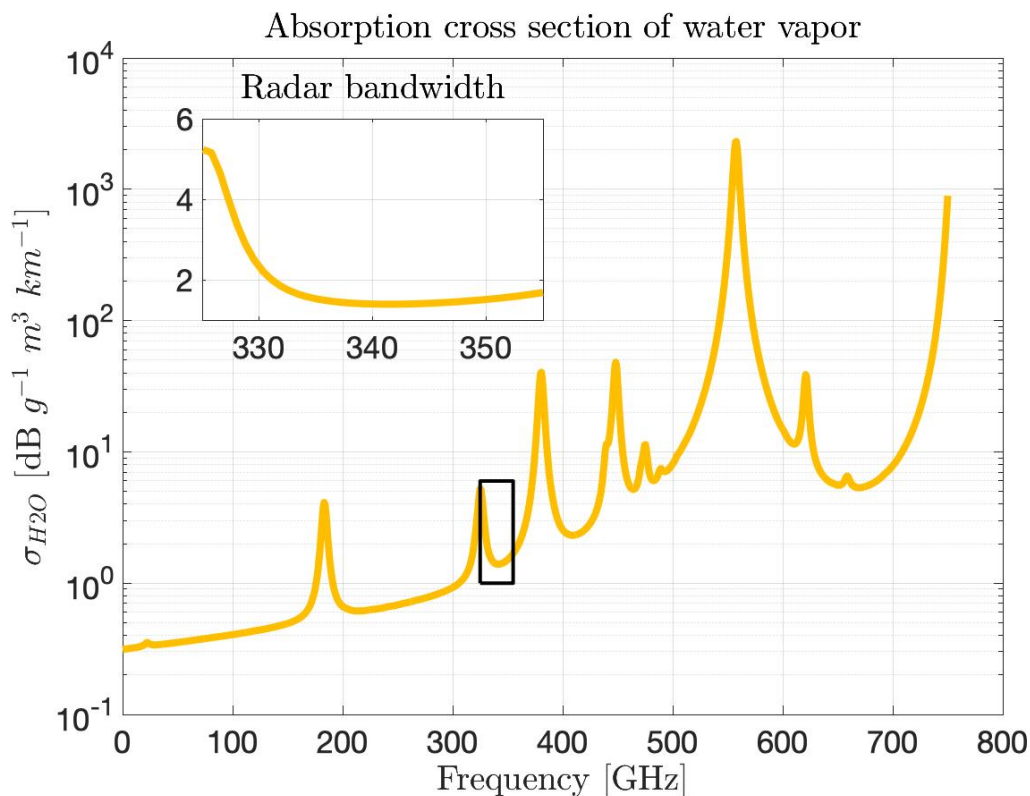


Figure 2.4: The absorption cross section of water vapor under normal atmospheric conditions ($P = 1 \text{ atm}$, $T = 290 \text{ K}$), in $\text{dBg}^{-1}\text{m}^3\text{km}^{-1}$, the inset shows the bandwidth of the radar used in this thesis.

2.3.3 Line by line approach

The extinction spectrum for a gas is calculated using Equation 2.10, which is a sum of N transitions each having a lineshape function (describing the shape of the transition in the frequency domain) described by a transition wave number ν_{ij} in cm^{-1} and scaled by a strength for the given transition S_{ij} [14]. The extinction is then scaled by the volume number density of the absorbing gas species $[X]$, in $\text{molecules}/\text{cm}^3$. Later the shape

2. Theory

of the lineshape and the temperature and pressure dependency of its parameters will be introduced.

$$\alpha(\nu) = [X] \sum_{n=1}^N S_{ij,n} f(\nu, \nu_{ij,n}, T, p) \quad (2.10)$$

The transition frequency ν_{ij} is constant but the lineshape itself contains a pressure dependent shift (see Equation 2.12) on the form $\delta(p_{REF})$, in cm^{-1} [14]. The line strength of a particular transition also has a temperature dependency, which is described in Equation 2.11. In which $Q(T)$ is the total internal partition sum for a given temperature, which is available from a HITRAN for each isotope, together with the needed constant c_2 , the lower state energy E'' measured in cm^{-1} is also listed for each transition [13] [14].

$$S_{ij} = S_{ij}(T_{ref}) \frac{Q(T_{ref})}{Q(T)} \frac{\exp(-c_2 E''/T)}{\exp(-c_2 E''/T_{ref})} \frac{1 - \exp(-c_2 \nu_{ij}/T)}{1 - \exp(-c_2 \nu_{ij}/T_{ref})} \quad (2.11)$$

The Lorentzian lineshape is derived from treating the excited molecules as electrical dipoles and thus with an exponentially decaying emitted field, the frequency domain representation of which is seen in the Lorentzian lineshape, which is shown in Equation 2.12 [14]. The Lorentzian line width γ_{ij} is described using Equation 2.13 [14] and its physical interpretation is that the dipole loses energy faster when interacting with nearby particles, thus this broadening is referred to collision or pressure broadening [2, Ch. 3]. This lineshape fits well to experimental data at higher pressures and lower temperatures, such as near ground atmospheric measurements [2, Ch. 3].

$$f_L(\nu, \nu_{ij}, p, T) = \frac{1}{\pi} \frac{\gamma_{ij}(p, T)}{\gamma_{ij}(p, T)^2 + [\nu - \nu_{ij} - \delta(p_{ref})p]^2} \quad (2.12)$$

$$\gamma_{ij}(p, T) = \left(\frac{T_{ref}}{T} \right)^{n_{air}} \left(\gamma_{air}(p_{ref}, T_{ref})(p - p_{self}) + \gamma_{self}(p_{ref}, T_{ref})p_{self} \right) \quad (2.13)$$

The parameters describing the line width γ_{ij} in air for a gas species are the self broadened width γ_{self} and air broadened width γ_{air} both at the reference temperature $T_{ref} = 290 \text{ K}$ and reference pressure $P_{ref} = 1 \text{ atm}$ as well as a parameter describing the temperature sensitivity for the gas species in air n_{air} [14]. The width is then a function of the partial pressure of air p_{air} and the gas species p_{self} , which are linked to the concentration of the absorbing gas species by the ideal gas law seen in Equation 2.14.

$$pV = nk_B N_A T \quad (2.14)$$

Ideal gasses are described by the ideal gas law, shown in Equation 2.14. Which contains the pressure p , volume V , amount in moles n , Boltzmann's constant k_B , Avogadro's number N_A and the temperature in Kelvin T . Assuming the gas mixture is a combination of air and another gas, then the ideal gas law can be re-written as shown in Equation 2.15. Where the pressure is divided into partial pressures depending on the mass concentrations ρ and molar masses M .

$$p = p_{air} + p_{gas} = \left(\frac{\rho_{air}}{M_{air}} + \frac{\rho_{gas}}{M_{gas}} \right) N_A k_B T \quad (2.15)$$

The Gaussian lineshape is derived from the Brownian motion of the absorbing molecules, where the velocity distribution in the direction of the wave vector \vec{k} gives rise to broadening from the Doppler effect which is referred to Doppler broadening [14]. The Gaussian lineshape is given by Equation 2.16, where ν_{ij} is the transition wavenumber and α_D is half-width at half-maximum of the Gaussian lineshape which can be calculated using Equation 2.17 [14]. This line shape works well in high temperature moderate pressures or lower pressures and moderate temperatures such as in the upper parts of the atmosphere [2, Ch. 3].

$$f_G(\nu, \nu_{ij}, T) = \sqrt{\frac{\ln 2}{\pi \alpha_D^2}} \exp\left(-\frac{(\nu - \nu_{ij})^2 \ln 2}{\alpha_D^2}\right) \quad (2.16)$$

$$\alpha_D(T) = \frac{\nu_{ij}}{c} \sqrt{\frac{2N_A k_B T \ln 2}{M_{gas}}} \quad (2.17)$$

The Voigt lineshape takes into account both collision broadening and Doppler broadening making it useful in cases where both effects are significant such as in a wave propagating from space to ground level. The Voigt line is formed by convolution the line shapes for the Lorentzian and Gaussian lineshapes, as seen in Equation 2.18 [14].

$$f_V(\nu, \nu_{ij}, P, T) = \int_{-\infty}^{+\infty} f_L(\nu - \nu', \nu_{ij}, P, T) \cdot f_G(\nu', \nu_{ij}, T) d\nu' = f_L(\nu, \nu_{ij}, P, T) * f_G(\nu, \nu_{ij}, T) \quad (2.18)$$

For this work all measurements and simulations were done at ambient temperature and pressure thus a Lorentzian lineshape, seen in Equation 2.12 is adequate however for future high temperature work a more advanced Voigt line shape as seen in Equation 2.18 may be of interest.

For calculating the absorption cross section of water vapor σ_{H_2O} Equation 2.10 was used, with data from [13]. Since the assumption in section 4.2 is that the partial pressure of water vapor $p_{self} = p_{H_2O}$ is negligible, the extinction spectrum $alpha(\nu)$ is calculated for $\rho \rightarrow 0 \text{ gm}^{-3}$ which is then converted to molecules per cubic meter to obtain $[X]$. Then the extinction spectrum α is used to calculate the absorption cross section $\frac{\alpha(\nu)}{\rho} = \sigma(\nu)$, then the frequency is re-scaled from ν in cm^{-1} to f in Hz.

3

Experimental setups

This chapter describes the various experimental setups including the radar that was used in this thesis. There were two series of experiments done, first with a fixed target and a gas cell in the path of propagation, this using the retrieval method described in section 4.1. Later is testing using the retrieval method described in section 4.2 shown, this by pouring particles through the path of the radar beam.

3.1 Radar configuration

In Figure 3.1 a simplified block diagram can be seen for the radar that has been used. The radar generates a low frequency chirp using a digital to analog converter (DAC), which is then mixed up to a higher frequency using microwave back-end electronics, which is then fed to the radar module. The radar module further up-converts the chirp until it reaches the final approx. 340 GHz. The terahertz signal is then coupled to collimating optics using a horn antenna. The intermediate signal from the radar module is then sampled by an ADC which is connected to the control computer.

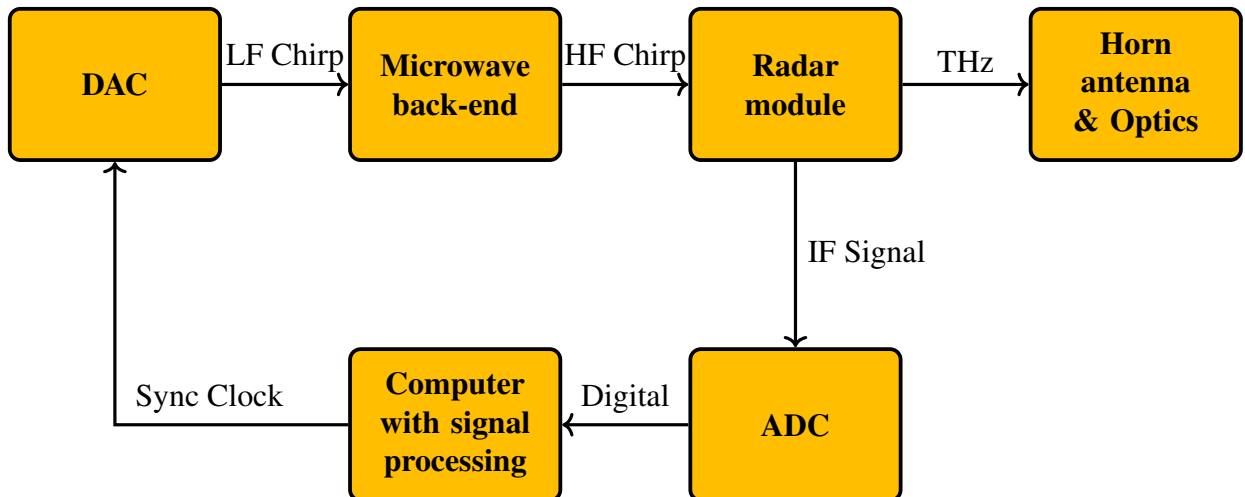


Figure 3.1: A simplified block diagram for the radar used in the experiments.

3.2 Experimentation with fixed targets

For testing with a fixed target a climate chamber, which can be seen in Figure 3.2 was constructed. It was constructed out of square aluminium tubing and high density polyethylene (HDPE) sheets as windows for the sides that the beam passed through, the remaining

3. Experimental setups

sides were covered in thin plastic to contain the humidity. Greater care was taken for the front/rear windows since a change in shape may change the propagation properties of the window, further HDPE was found to offer low attenuation and reflectivity for THz frequencies compared to the thin plastic that was used.

The angle of incidence was slightly off-set from right angle, this to drastically reduce window reflections as they would interfere with desired reflections as well as increase the noise floor. This was used for both windows. For tests using no window the plastic film was used with cut outs for the beam, to remove any effects of the windows. For monitoring the humidity a hygrometer was used, which was placed inside the chamber. The humidity was changed by spraying mist into the chamber.

The target was a ≈ 5 mm diameter metallic sphere suspended in air using a wooden pole and a XY translator for precision alignment with the beam pattern, the target was placed in front of a leaning piece of sheet metal to act as a mirror to reduce background reflections. Other targets were also experimented with, however only data for the metallic sphere is shown in section 5.1.

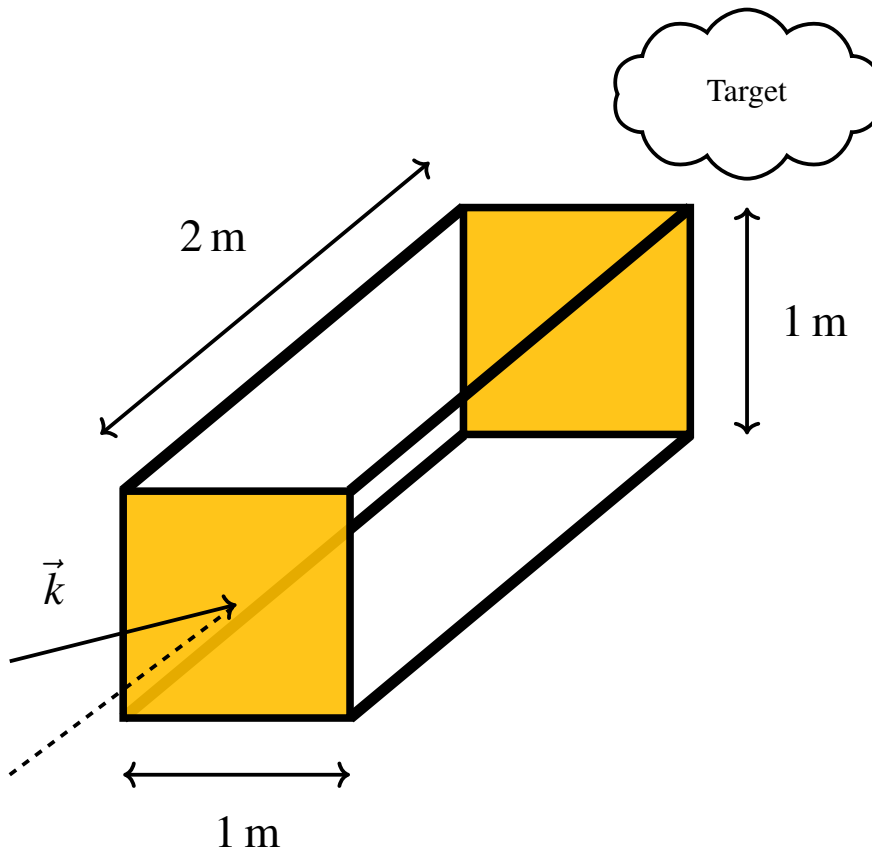


Figure 3.2: The experimental setup used for fixed target measurements. The chamber allows for controlling the water vapor concentration in the path of the beam.

3.3 Experimentation with falling particles

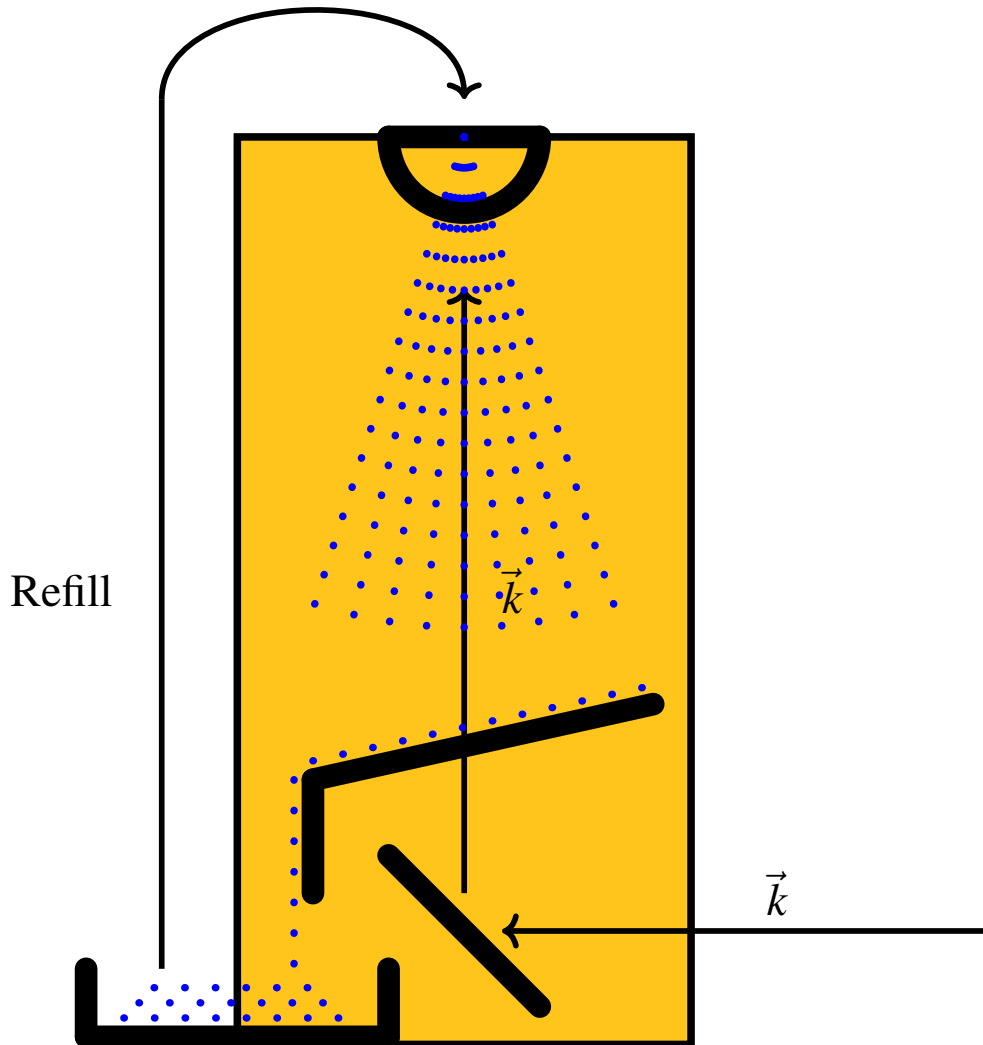


Figure 3.3: Test setup for falling particles

For tests using falling particles, a setup as shown in Figure 3.3, which consists of a frame holding a sift above a semi-transparent tray that collects the falling particles and channels them into a another tray for re-use. The setup is further dressed in paper sheets to reduce spillage of particles. The beam of the radar enters orthogonal to the fall path and is reflected by a mirror to travel in-line with the falling particles, thus monitoring the extinction through the cloud under the sift.

The particles used for the experiments were glass particles of type: 212-250 micrometer diameter Ballotini, the dielectric constant ϵ_r is assumed to be equal to 6 using [15]. This size was chosen due to availability of large amounts of media since long measurements were required. The particle size was also a good choice based on the reasonable back scatter efficiency of the particles, however metallic particles could offer better values. The size distribution of the particles used in the calculations of extinction cross section was

3. Experimental setups

chosen as a single particle size with the diameter of the center diameter of the distribution of the real particles.

4

Retrieval methods

This chapter describes the methods used in the two experiments to retrieve the water vapor concentration of the air, first in section 4.1 a more empirical method is proposed and later a more theoretical method is formulated in section 4.2 and then a simulation method for it in section 4.3. In the context of this thesis a retrieval method is a method that uses the radar measurements to estimate the humidity and particle concentration of the environment, but also possibly more outputs.

4.1 Water vapor retrieval from fixed target

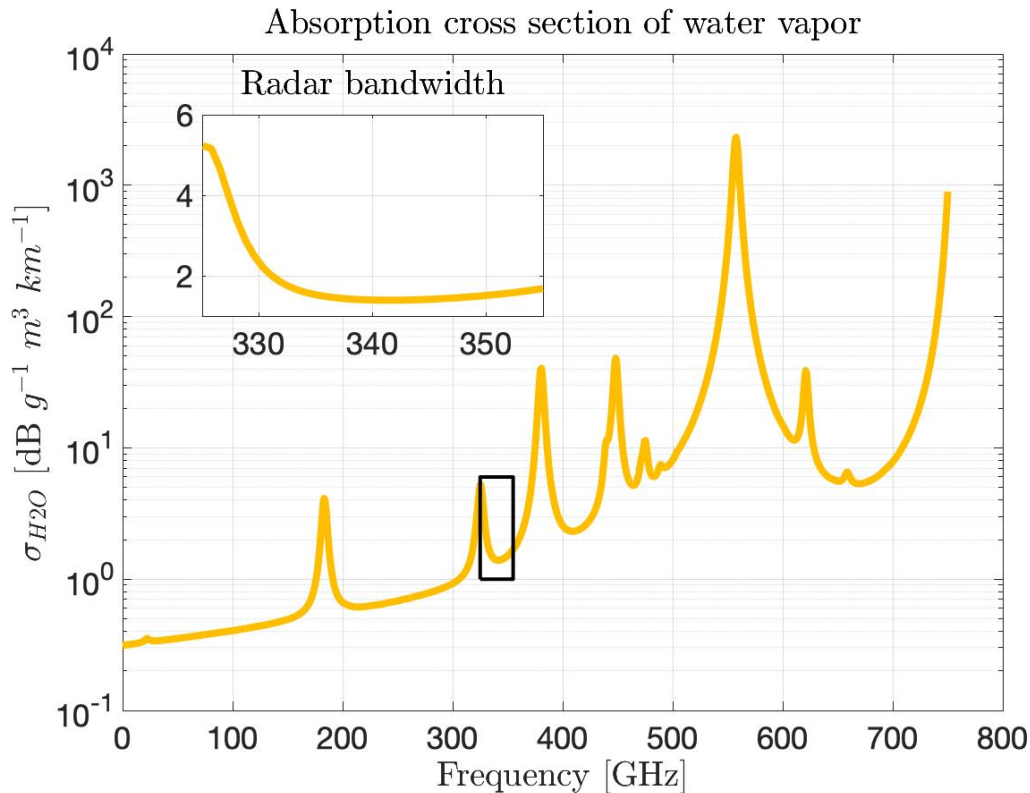


Figure 4.1: The absorption cross section of water vapor under normal atmospheric conditions ($P = 1 \text{ atm}$, $T = 290 \text{ K}$), in $\text{dB g}^{-1} \text{m}^3 \text{km}^{-1}$, the zoomed-in section is for the bandwidth of the radar used in this thesis. The attenuation is varying and steadily increasing with absorption peaks at certain frequencies.

The goal with this method is to investigate if the ratio between the high and low frequency measurements of the radar can be correlated to the water vapor concentration inside of a gas cell, rather than estimate humidity directly. This is done using signal processing to obtain this ratio, which is shown in Figure 4.2. The signal processing begins by dividing the chirp time series in two, to form a low and high frequency reading s_l and s_u . This is done since the low frequency part of the bandwidth should have higher attenuation than the upper part of the bandwidth, as seen in Figure 4.1. These signals are then coherently integrated to increase the signal to noise ratio, then a hamming window is applied and the signal is Fourier transformed to obtain a range profile for the low and high frequency reading. Then a moving mean is applied to reduce the fluctuations of the measured powers which are then divided by each other and converted to decibels for a reading of the low/high ratio R_{dB} for a certain distance and a few surrounding range indices, the time series of which is saved for comparison with readings from a hygrometer that measures the water vapor concentration.

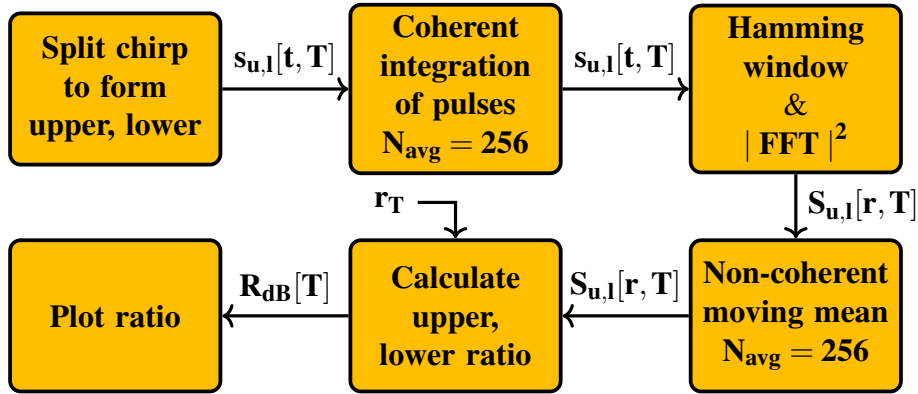


Figure 4.2: The block diagram of an equivalent signal processing chain to the one used, simplified to omit unrelated parts of the chain. Fast time index is t , slow time is T and distance to target monitored is r_T .

4.2 Water vapor retrieval in particulate medium

This section describes the method used to retrieve a water vapor profile from radar data and the underlying assumptions that are done, as well as the signal processing that precedes the retrieval method. The method presented is heavily inspired and aided by the retrieval method used in NASA's VIPR project [6], this work does however solve for different state variables as it not only retrieves humidity but also particle concentration.

4.2.1 Assumptions and conditions

In order to synthesize a retrieval method the problem needs to be defined and constrained, these constraints are discussed and presented below.

Gas absorption It is assumed that only water vapor shows a clear frequency dependent shape. Background gases may attenuate, however they would show little to no contrast over frequency and thus not be distinguished against a range dependent loss of power. In section 2.3 it is shown that the actual absorption cross section of a gas is dependent on the

other gases in the mixture as well as temperature, partial pressures of the different gases. A reasonable approximation would be to assume that the gas mixture is simply water vapor and air and that the partial pressure of water vapor is much lower than that of the air. This is true for atmospheric pressure and ambient temperature which is a good assumption as the tests would be done under normal atmospheric conditions. These assumptions would result in an absorption cross section of water vapor that is approximately a function of frequency only, thus using section 2.3 the cross section is calculated using $T = 290\text{ K}$ and $P = 1\text{ atm}$ for the center frequency of each sub-band.

Particles in the environment The particles in the path of the radar beam are of utmost importance as their extinction cross-section allows estimating their concentration in the same fashion as the water vapor concentration will be estimated. The particles available are spherical and are made of glass, with various size distributions. For a simple test and lack of exact method to measure the concentration of particles, a simple approximation will be used. The particles are assumed to be of the same size, which is the mean of the size distribution of the particles used. Thus this model does not work well for particles of widely varying size, as very small particles show a Rayleigh type behavior compared to larger which might have a Mie behavior. The code [12] is used to calculate the back-scatter and extinction cross-sections for use in the model, this at the center frequency of each sub-band.

4.2.2 Radar processing

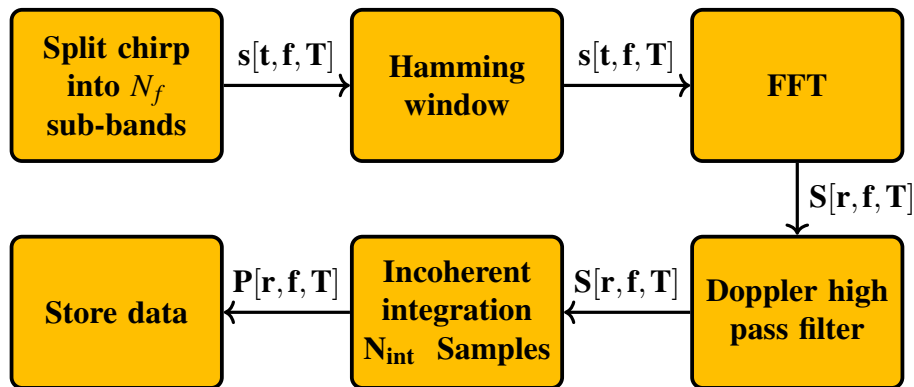


Figure 4.3: The block diagram of an equivalent signal processing chain to the one used, simplified to highlight the main steps. Fast time index is t , frequency is f and slow time is T . All steps are done independently for each sub-band.

The block diagram of the signal processing done before applying any retrieval method is shown in Figure 4.3, which consists of dividing the chirp into multiple sub-bands for different frequency points, then each sub-band is processed separately. The next step is to apply hamming windows onto each sub-band, followed by Fourier transforming the fast time signal to obtain a range profile for each sub-band. Then a Doppler high pass filter is applied to remove stationary targets, which arise from reflections of the test setup, the cut-off frequency and filter order of which was adjusted so that no stationary targets were seen in a range-Doppler plot. The removal of stationary targets is important since

they would not fit the model, as it assumes only particles of a uniform size but randomly changing phase. After the filtering, the sweeps are in-coherently integrated to yield a power estimation $P[r, f, T]$ before finally being stored for further analysis. Worth noting is that a portion of the sub-bands were skipped in the retrieval method as they are outside of the radar module’s design frequency span or corrupted by a hardware glitch. Further measurements where the received power for all analyzed ranges and frequencies was not greater than 3 dB from the noise floor were dropped in experiments, this as to not process data with undesirable quality. The noise floor level was approximated as flat over range and frequency, with a good fit for most of the analyzed range indices.

The radar settings used in the experiments with falling particles in section 5.2 are as shown in Table 4.1.

f_0	BW	N_f	D	ϵ_r	P	T	$\frac{N_{ind}}{T_{int}}$
340 GHz	25.6 GHz	25	231 μm	6	1 atm	290 K	1024 Sa s^{-1}

Table 4.1: The different parameters used for the measurements shown in section 5.2. Where f_0 is center frequency, BW the total bandwidth, N_f the number of frequency points, D diameter of particles in model, ϵ_r relative permittivity of particles in model, P the ambient pressure, T the ambient temperature and $\frac{N_{ind}}{T_{int}}$ the number of statistically independent measurements per second of integration.

4.2.3 Retrieval method

The retrieval method will use the multi frequency radar measurements of the reflected power from different ranges and frequencies $P(r, f)$, this to estimate the state variables, water vapor concentration over range $\rho(r)$, particle concentration over range $n(r)$ and a proportionality constant $k_r(r)$. The latter being a free parameter used in differential absorption spectroscopy [2, Ch. 6] that will include things such as absolute output power, IF filter response and therefore this method should be robust to changes in the output power and IF filter shape. For example it should be capable of working with and without a window in-between the radar and particle cloud as the attenuation by the window is not important since no absolute quantities are needed.

The method proposed below is heavily inspired by [6], which in turn is based on material from [16]. The difference between this retrieval method and [6], is the addition of particle concentration as a state variable as it is of interest for this work as well as the omitting of the regularization technique used in [6].

This retrieval method is a so called inversion technique which is essentially a curve fit of a model of the physics and radar characteristics(in this case) called a forward model onto the measurements, resulting in an estimate of the unknown state variables [16, Ch. 2]. To do this one must first create a truthful forward model, that includes known unknowns such variations in the radar characteristics. This starts with the radar equation shown in Equation 4.1. Which has been modified to have a Swerling type 2 back-scatter cross section $\langle \sigma_{cloud}(r, f) \rangle$ as described in subsection 2.1.3, this as the particles are a valid example of a Swerling-2 target. The radar equation has further been modified with

an unknown term that describes the range varying conversion factor from output to power measurement $K_r(r)$, that for example can describe how the IF electronics may attenuate some ranges more than others or absorption by a gas with little to no spectral contrast in the bandwidth of the radar. An additional unknown term that describes the conversion factor from sent power to measured power over frequency is also added $K_f(f)$, which can describe the frequency varying output power, antenna gain or similar. These unknown terms represent the behavior the radar that may drift over time and thus not be reliable or stable enough to calibrate, for example how the frequency response of an IF amplifier changing over time may change K_r . The brackets $\langle \rangle$ represent to the time average of the enclosed variable.

$$\langle P_{rec}(r, f) \rangle = P_t \frac{G_{antenna}^2 \lambda^2}{(4\pi)^3 r^4} K_r(r) K_f(f) \langle \sigma_{cloud}(r, f) \rangle \quad (4.1)$$

The average radar cross section of the particle cloud from a certain range and frequency $\langle \sigma_{cloud}(r, f) \rangle$ is assumed to be equal to Equation 4.2. Where $V_{scatter}$ is the scattering volume which describes the volume of range index (roughly equal to the range resolution times the area of the beam at distance r), the number of particles per volume $n(r)$ at range r and the backscatter cross section of a single particle $\sigma_b(f)$ [8, Ch. 19].

$$\langle \sigma_{cloud}(r, f) \rangle = V_{scatter} n(r) \sigma_b(f) \quad (4.2)$$

Now these equations may be combined as seen in Equation 4.3, where the conversion factors K_r and K_f can be made to include most of the terms from the radar equation, as seen in the right hand side of Equation 4.3. Since no absolute values of any power is used because of the unknown conversion factors, there is no value in keeping most of the terms from Equation 4.1 and Equation 4.2.

$$\langle P_{rec}(r, f) \rangle = K_r(r) K_f(f) n(r) \sigma_b(f) \quad (4.3)$$

Now the extinction by particles and absorption by water vapor may be added, which is done using Beer-Lamberts law as seen in subsection 2.3.1 and using the physics in section 2.2. The total attenuation from the radar to the target and back is represented by the addition of the integral in Equation 4.4, where $\sigma_{ext}(f)$ is the extinction cross section of the particles, $\sigma_{H_2O}(f)$ is the absorption cross section of the water vapor in air and $\rho(r)$ is the water vapor concentration at range r . These extinctions will provide a contrast in both range r and frequency f and thus should not be confused with the unknown conversion factors $k_r(r)$ and $k_f(f)$, and therefore allow for estimations of the concentrations $n(r)$ and $\rho(r)$.

$$\langle P_{rec}(r, f) \rangle = K_r(r) K_f(f) n(r) \sigma_b(f) \exp\left[-2 \int_0^r (n(r') \sigma_{ext}(f) + \rho(r') \sigma_{H_2O}(f)) dr'\right] \quad (4.4)$$

To compress the equations the notation is changed to $P(r, f) = \langle P_{rec}(r, f) \rangle$. The next step is to take the natural logarithm of Equation 4.4 as it would make the observable (received power) linear with respect to the state variables $n(r)$ and $\rho(r)$, although with the exception of the term $\ln(n(r))$ which will be discussed later. This is shown in Equation 4.5.

$$\begin{aligned} \ln(P(r, f)) &= \ln(K_r(r)) + \ln(K_f(f)) + \ln(n(r)) + \ln(\sigma_b(f)) \\ &\quad - \int_0^r 2[\rho(r')\sigma_{H_2O}(f) + n(r')\sigma_{ext}(f)] dr' \end{aligned} \quad (4.5)$$

The next step is to make Equation 4.5 a linear equation by taking the logarithm of it and then discretize it for each step in range and frequency, which are done at a granularity of their resolutions ΔR , Δf similarly to [6]. Equation 4.5 is almost a linear function of the state variables: $K_r(r)$, $n(r)$ and $\rho(r)$, with the exception of the $\ln(n(r))$ term. Since the proportionality constant K_r is a degree of freedom and does not produce information of interest one can opt to include the $\ln(n(r))$ term in it and thus making the equation linear with respect to the state variables. The frequency calibration constant K_f can be ignored and set to be 0, as applying a least-squares fit of Equation 4.5 to this model will yield the same state variables irrespective of the actual value of K_f (this was tested). This yields Equation 4.6, which is more easily represented in new notation where $X_y(r_i, f_j)$ is replaced with $X_y^{i,j}$.

$$\ln(P^{i,j}) = \ln(K_r^i) + \ln(K_f^j) + \ln(\sigma_b^j) - 2\Delta R \sum_{k=1}^i \left[n^k \cdot \sigma_{ext}^j + \rho^k \cdot \sigma_{H_2O}^j \right] \quad (4.6)$$

The next step to obtaining the state variables is to invert the problem, a least-square fit is used since the problem is over-determined with $3 \times N_r$ unknown values and $N_r \times N_f$ measurement points, where N_r, N_f is the number of range and frequency indices respectively. One wants to describe Equation 4.6 in the form of a linear equation system as seen in Equation 4.7, where the state variables are defined inside x a column vector of length $3 \times N_r$ as seen in Equation 4.9 and the measurement data points in y a column vector of length $N_f \times N_r$, on the form seen in Equation 4.8, just as shown in [6].

$$y = Ax + b \quad (4.7)$$

$$y = \ln \begin{bmatrix} P_r^{j=1} \\ P_r^{j=2} \\ \vdots \\ P_r^{j=N_f} \end{bmatrix} \quad (4.8)$$

$$x = \begin{bmatrix} \ln(K_r) \\ n \\ \rho \end{bmatrix} \quad (4.9)$$

The matrix A and column vector b will contain the information regarding the physics of the problem, b will contain the back-scatter cross-section information as seen in Equation 4.11 while A contains how the received power depends on the state variables. A is a $(N_f \cdot N_r) \times (3 \cdot N_r)$ matrix, defined as seen in Equation 4.10, where I_{N_r} is a identity matrix of size $N_r \times N_r$, T_{part} and T_{H2O} are the optical depth matrices for particles and water vapor respectively. The matrices are assembled as shown in [6].

$$A = \begin{bmatrix} I_{N_r}, & -T_{part}(f_1), & -T_{H2O}(f_1) \\ I_{N_r}, & -T_{part}(f_2), & -T_{H2O}(f_2) \\ \vdots & \vdots & \vdots \\ I_{N_r}, & -T_{part}(f_{N_f}), & -T_{H2O}(f_{N_f}) \end{bmatrix} \quad (4.10)$$

$$b = \begin{bmatrix} \left(K_f^{j=1} + \ln(\sigma_b^{j=1}) \right) \vec{1}_{N_r} \\ \left(K_f^{j=2} + \ln(\sigma_b^{j=2}) \right) \vec{1}_{N_r} \\ \vdots \\ \left(K_f^{j=N_f} + \ln(\sigma_b^{j=N_f}) \right) \vec{1}_{N_r} \end{bmatrix} \quad (4.11)$$

The optical depth matrices are defined as seen in Equation 4.12, 4.13, where L_{N_r} is a lower triangular matrix of size $N_r \times N_r$, σ_{ext} the extinction cross section of the particles used, σ_{H2O} the absorption cross section of water vapor and ΔR the range resolution of a sub-band as seen in subsection 2.1.5. This matrix formulation is similar to that used in [6], but includes the extinction from particles. The function of the lower diagonal

matrix is to act as the sum which is a discrete integration, meaning r_i has the accumulated extinction/absorption of range cells numbering r_1, r_2, \dots, r_{i-1} .

$$T_{part}(f_j) = \Delta R \cdot \sigma_{ext}(f_j) 2L_{N_r} \quad (4.12)$$

$$T_{H2O}(f_j) = \Delta R \cdot \sigma_{H2O}(f_j) 2L_{N_r} \quad (4.13)$$

The problem can be solved by minimizing the least squares error between the data and the model, however since the data points may have a greater or less uncertainty it is vital to weight the errors according to the noise of the data. Having information regarding the uncertainty of each data point also allows one to estimate the uncertainty of the estimated result, which is quite useful. To do this one needs a model of the noise, for this work that model is borrowed from [6], although with an assumption and slight change in notation. Information regarding the noise model used is found in section A.1.

The noise weighted least squares estimation of the vector containing the state variables \hat{x} is done using Equation 4.14 [6], where S_y and S_e are the co-variance matrices that describe the model of the noise found in section A.1. The estimated co-variance matrix of the estimated state vector \hat{S}_x is given by Equation 4.15 [6], for visualizing uncertainties the diagonal values are used as the variance of each retrieved value.

$$\hat{x} = \left[A^T (S_y + S_e)^{-1} A \right]^{-1} A^T (S_y + S_e)^{-1} (y - b) \quad (4.14)$$

$$\hat{S}_x = [A^T (S_y + S_e)^{-1} K]^{-1} \quad (4.15)$$

4.3 Simulation of expected performance of retrieval method

This section describes the approach used for simulating the expected performance of the retrieval method in a particulate medium, this to determine the feasibility of using this approach in a process reactor. The code for which can be found in section A.2.

The simulation starts with defining the characteristics of the radar such as: center frequency f_0 , total bandwidth BW , number of frequency points (thus also range resolution) N_f , number of range indices to simulate N_r , number of independent samples gathered N_{ind} . Further a single size of particle of diameter D and dielectric constant ϵ_r is assumed and used together with Mie-theory to calculate the back-scatter, extinction cross sections. For gas absorption only water vapor is assumed, the absorption cross section generated using the data from HITRAN is used, at the assumed pressure and temperature, for these 1 atm and 290 K was used respectively.

The next step is to analytically define a true distribution for the particle concentration $n(r_i)$ and water vapor concentration $\rho(r_i)$ as well as a constant scaling of the received power. The received power is then calculated using the forward model used in the retrieval method, although afterwards correcting for the $\ln(n(r_i))$ and adding a $-4\ln(r)$ part to simulate the radar equation, something the model of the retrieval method ignores. The next step is to use the "true" power to generate a noise model and then use it to add sufficient noise onto the "true" power to have a simulation of the received power according to the model, this is done directly on the y vector and thus it does not simulate well for extreme amounts of noise as it does not simulate the step of $y = \ln(P)$.

Now the noisy measurement vector y can be used together with the retrieval method to compare the true and retrieved profiles, as the simulated data is produced using the forward model this simulation only allows one to estimate the necessary integration time. Further since a proportionality constant is used (and not known for the radar) it does not simulate the lack of received power from a too thin distribution of particles, as the reflected power will be too low.

f_0	BW	N_f	D	ϵ_r	P	T	$\frac{N_{ind}}{T_{int}}$
340 GHz	25.6 GHz	25	231 μm	6	1 atm	290 K	1024 Sa s^{-1}

Table 4.2: The different parameters used for the simulations shown in section 5.3. Which include the center frequency of the radar f_0 , the total bandwidth of the radar BW , the number of frequency points N_f , the diameter of the particles measured D , the dielectric permittivity of the particles ϵ_r , the ambient pressure P , the ambient temperature T and the number of statistically independent samples per second of integration $\frac{N_{ind}}{T_{int}}$.

4. Retrieval methods

5

Results

This chapter describes the results that were obtained from experiments with fixed targets and falling particles, further simulations to estimate the feasibility of estimating humidity using a particulate medium.

5.1 Experimentation with fixed target

Measurements using the fixed target setup described in section 3.2 were done both using a HDPE window and using a plastic film window with a cut-out for the beam. An example of a comparison between the radar low / high frequency ratio in decibels and the hygrometer water vapor concentration in units of g m^{-3} can be seen in Figure 5.1, this using a HDPE window and a 5 mm diameter metal sphere as the target. In the figure a clear correlation between the radar measurement and hygrometer reading is seen, although with slight drift of the radar ratio over time.

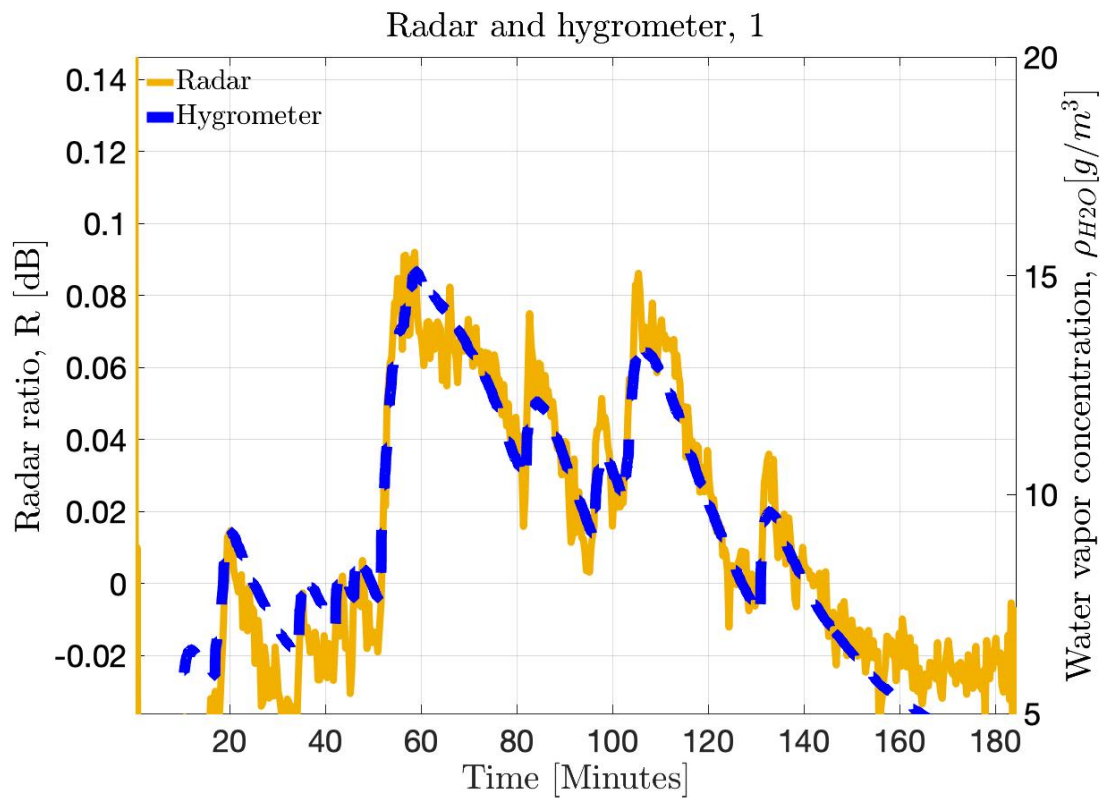


Figure 5.1: A time series comparison between the radar high/low frequency ratio, R and the hygrometer's water vapor concentration reading. It can be observed that there is a strong correlation between the humidity reading and the radar reading, although drift is also noticeable.

The measured ratio can then be plotted against water vapor concentration to achieve a scatter plot where a linear fit is applied, this using 40 times down-sampled data for easier viewing, the same data can then be seen in Figure 5.2. Here a linear relationship can be observed, which is expected as the ratio is in units of decibels, the slope of which will depend on the absorption cross section and gas cell length. The linear fit and its estimated slope, something that should be consistent with gas-cell length irrespective of target type or position, this slope in units of $dBm^3 g^{-1}$ and how it changed for different scenarios is of importance to evaluate the method.

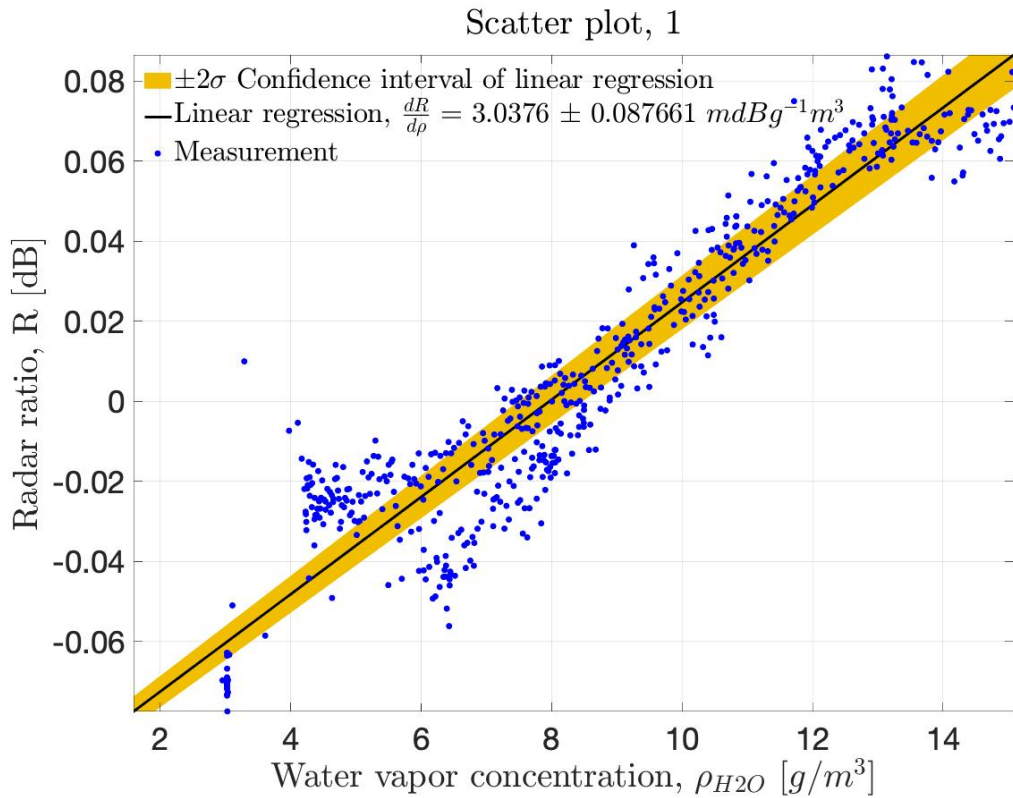


Figure 5.2: A scatter plot comparison between the radar high/low ratio and the hygrometer’s water vapor concentration reading, a clear linear relation is observed with a measured slope displayed in the legend of the figure. The drift over time seen in Figure 5.1 can be seen as there appears to be two different lines merging into one.

Several different targets were used and produced very different slopes and with different consistencies. Some of the targets showed large instabilities and would not reach a fixed initial value for the ratio, others like a metallic rod standing up showed strong angle dependency for the initial humidity value. For the metallic rod target the slope showed a variation of the slope of more than a magnitude, thus slightly changing the angle of the rod could completely change the strength of the measured effect showing another phenomenon than simply water vapor absorption was observed. Similarly the metallic sphere also showed a large dependency of the exact position of the sphere in the beam, further the slope was also inconsistent to around a magnitude in-between different positions. These inconsistencies were observed both with and without the cut-out in the windows. For the sphere specifically a note was also made that the slope inconsistency increased when the angle went further from normal incidence in the path of propagation and height plane, but only for the HDPE windows not for the cut-out setup. This suggesting that the windows were bending the beam and thus hitting the target differently at different frequencies and that this behavior had a dependency on the water vapor concentration inside the gas cell.

A hypothesis for an explanation of these two effects for the case with windows is that the beam is deflected according to Snell’s law [17, Ch. 7] and thus the direction of the beam will depend on the refractive index inside and outside the chamber. The imaginary part of the refractive index is the loss of the medium, thus it will depend on the water vapor

concentration and frequency as the absorption per length does. Then arguing from the Kramer-Kroenig relations [17, Ch. 1], the real part of the refractive index will depend on the imaginary part of the refractive index and thus also depend on frequency and humidity, therefore offering an explanation why the behavior changes with the water vapor concentration. For the hole in the window case the slope is still not consistent and a hypothesis is that there is a gradient of water vapor inside the chamber and again arguing from the Kramer-Kroenig relations there should be a gradient of refractive index, something that can bend a plane wave [17, Ch. 7] and thus alter the angle of the beam. The changed angle of the beam will change the amount of power reflected since the target is more/less in the path of the beam, something that was also observed.

A way to fix this would be to use a target that is independent to angle of incidence or position, such as a target with diffuse scattering. While diffuse scatters were experimented with, none gave promising results. Instead a conclusion can be formed that something like a cloud of particles is promising.

5.2 Experimentation with falling particles

This section shows a portion of the results obtained using the experimental setup described in section 3.3 which are then in turn analyzed using the retrieval method described in section 4.2. Since the integration time is rather limited, the total accumulated integration time is a mere 48.5 s, thus expectations for humidity measurements are not high if one compares to the simulations in section 5.3. Instead there is hope to detect a somewhat stable time averaged particle concentration over range(it will fluctuate over time as the pouring is not stable) and that the time averaged humidity over range is spread out around 10 gm^{-3} within the estimated uncertainty.

By time averaged one means the standard deviation weighted mean of all measurements over time, calculated for each range index. The over time values for each range index are controlled to not contain outliers as they could result from a poor model fit, something that might not be reflected in the estimated uncertainty.

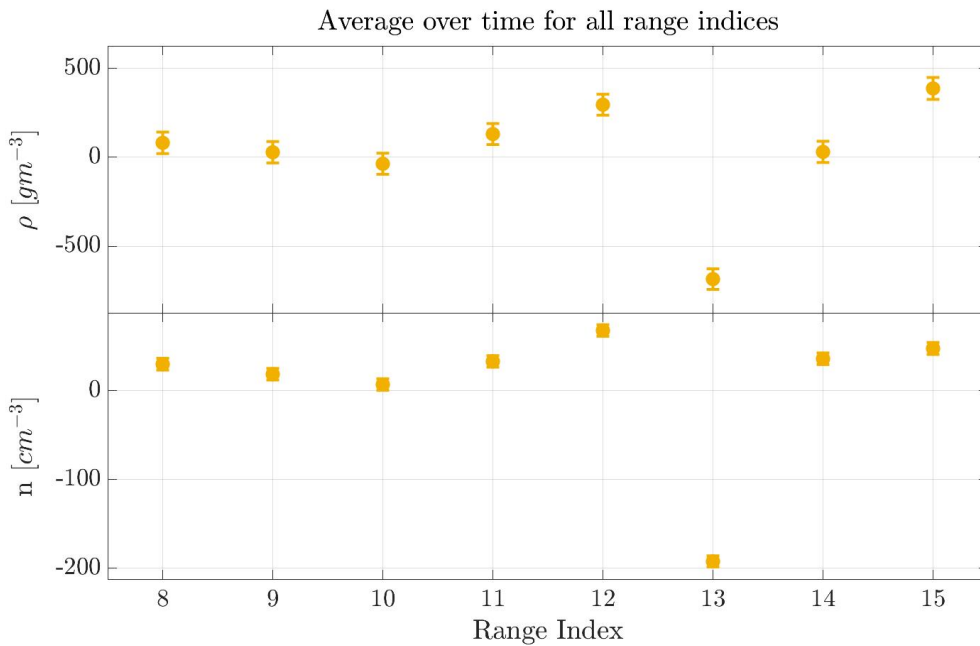


Figure 5.3: The full range span measurement of the time-averaged water vapor ρ and particle concentration n , the data is shown with error bars marking the 1σ uncertainty. The readings are somewhat constant with the exception of an out-liar at range index 13.

The full range span measurement is shown in Figure 5.3, where the data for both water vapor and particle concentration is somewhat constant with the exception of an out-liar at range index 13. This could be explained by RF-leakage from the radar electronics into the IF signal thus adding interference at a certain range index, as has been noticed in previous experiments. The values at the higher ranges are near the strongly reflecting nozzle of the

setup and thus could cause signals not modeled by the retrieval model and throw off the estimations, this assuming the Doppler filter is not 100% effective. Therefore the analysis will instead focus on the closer range indices: 8 – 11 which are further from the nozzle and the interference source, here the model should fit better as the particles are the furthest from fixed targets as possible. Instead of simply cropping the data will be reanalyzed and only samples with too low SNR inside the optimal range indices will be thrown, this to obtain a longer integration time.

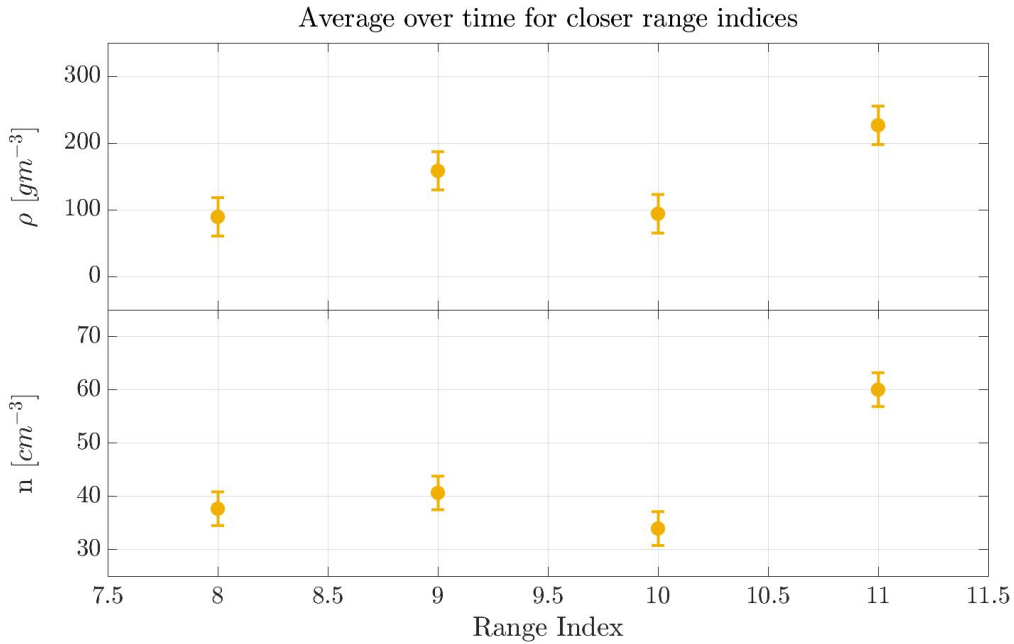


Figure 5.4: The optimal range span measurement of the time-averaged water vapor ρ and particle concentration n , the data is shown with 1σ uncertainty as error bars. The readings are more consistent compared to the full span.

The time averaged values of range indices 8 – 11 are seen in Figure 5.4, here a much better consistency can be seen. The particle concentration yields a finite value in the order of $\hat{n} \approx 30 \text{ cm}^{-3}$ and the humidity measurements are around 100 gm^{-3} ($\approx 10\times$ too high). Worryingly the humidity values seem to mimic the spread of the data points for particle concentration, perhaps the model is not fitting well enough. A miss alignment in frequency and very weak water vapor absorption (which is true in this case) could cause the model to confuse particle extinction and humidity while preserving a reasonable fit. The bad fit for humidity suggests controlling the radar setup further and then testing in an environment with more humidity to more clearly resolve the absorption from water vapor.

To estimate the reason-ability of the particle concentration estimate, one can assume constant flow of falling particles with a speed of around 5 m s^{-1} in the shape of column with area approximate that of the beam and height of the experimental setup. Using this one

can calculate the total mass of the particles fallen ($\approx 3 \text{ kg} \times N_{refills} \approx 30 \text{ kg}$) using the total time of the experiment and mass of the assumed particle. The calculations essentially approximates the mass using the mass of a column of particles times the total amount of columns that could have fallen during the time of the experiment, as seen in Equation 5.1.

$$m_{tot} \approx T_{experiment} \times \hat{n} m_{particle} A_{beam} \times \frac{V}{h} \quad (5.1)$$

T_{exp}	\hat{n}	A_{beam}	$V_{particle}$	h	$m_{particle}$	$m_{estimated}$
370 s	40 cm^{-3}	20 cm^2	500 cm s^{-1}	100 cm	$1 \times 10^{-8} \text{ kg}$	100 kg

Table 5.1: The factors used to estimate the total mass fallen during the experiment m_{tot} using the length of the experiment T_{exp} , estimated time average particle density \hat{n} , approximate area of beam A_{beam} , approximate velocity of particles $V_{particle}$, approximate height of experimental setup h and the approximate mass of a single particle $m_{particle}$.

Using Equation 5.1 the numbers in Table 5.1 yields an estimated total fall mass of around 100 kg, within one magnitude of the expectation. Thus the particle estimation part of the result can be seen as promising and in demand of further testing, this using more attention to the details of the experiment. Since the water vapor estimate is built on the same type of measurement but using much lower values of extinction one can expect the water vapor measurements to improve with higher levels, thus providing stronger extinction.

5.3 Simulation of expected performance in a particulate medium

This section describes the simulations that were done which evaluate the performance of the retrieval method described in section 4.2, this using the method described in section 4.3. The first point of interest is to figure out at what order of integration time can measurements of the humidity be achieved in room temperature conditions ($\rho < 20 \text{ g m}^{-3}$), since this is easier to test. The second point would be to figure out at around what magnitude one could possibly achieve performance satisfactory for a process reactor where the humidity is in the order of hundreds of grams.

In Figure 5.5, 5.6 and 5.7 is a comparison between the "true" and retrieved particle and water vapor concentration profiles, this with 0.1, 10 and 200 s of integration time respectively. Focusing on the ability to retrieve humidity it is clear that video-rate speeds of 0.1 s is not achievable, however at more modest integration times of 10 s the humidity uncertainty is perhaps sufficient to be usable in an environment with many hundreds of g m^{-3} of water vapor. It is also evident that measuring room temperature levels of humidity will require integration times in the order of minutes, at these settings.

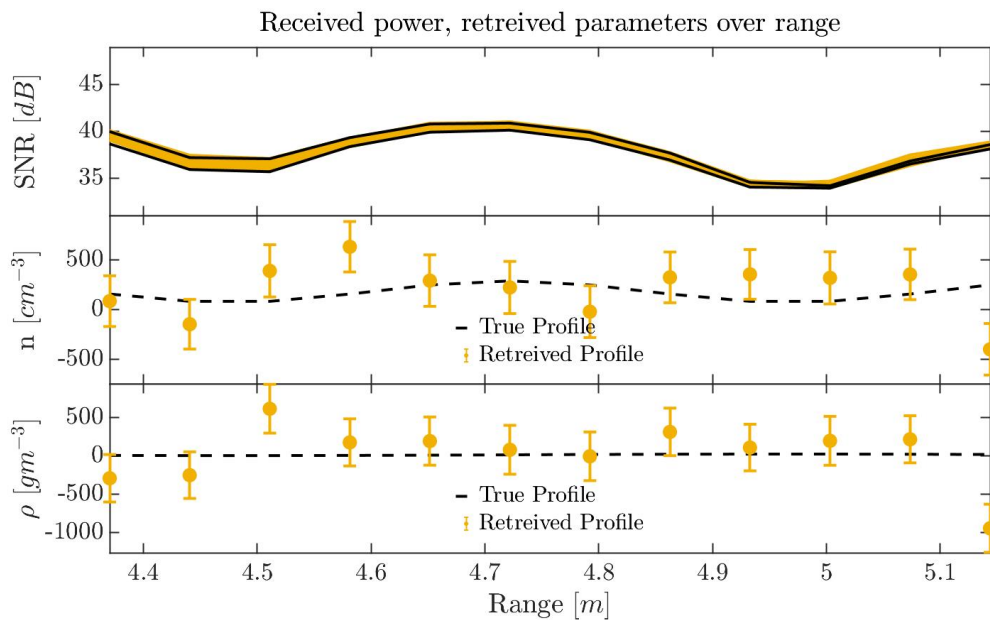


Figure 5.5: A comparison between the true and retrieved particle and water vapor concentration profiles, this with an integration time of 1 sec. For this short of an integration time both particle and water vapor concentration is very uncertain. The SNR is also shown over range for all the different frequencies.

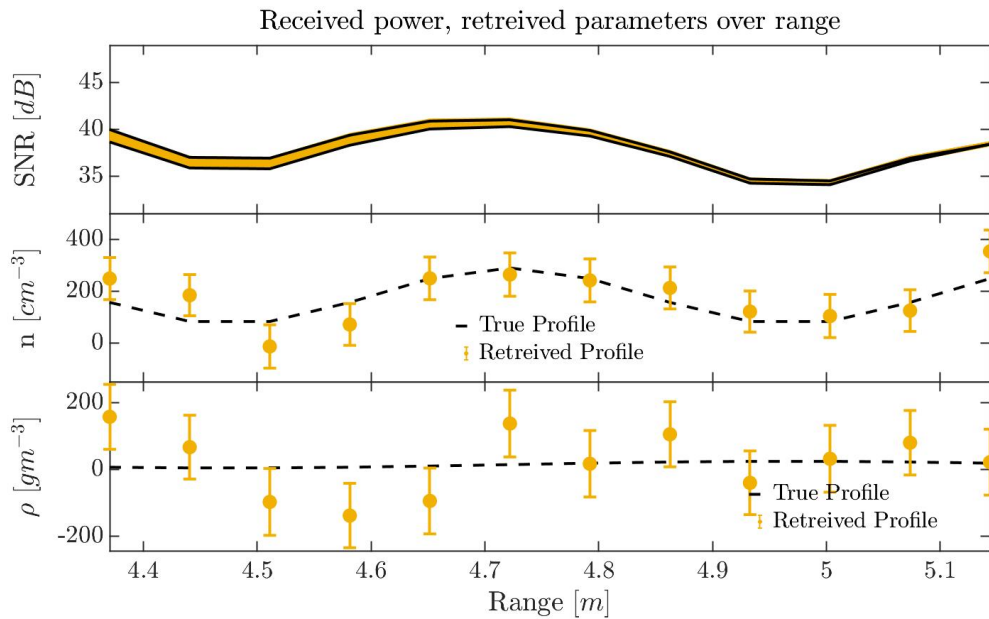


Figure 5.6: A comparison between the true and retrieved particle and water vapor concentration profiles, this with an integration time of 10sec. At this long of an integration time the particle concentration is becoming increasingly accurate while the humidity is still not good enough for room temperature humidity, but could be useful at much higher concentrations. The SNR is also shown over range for all the different frequencies.

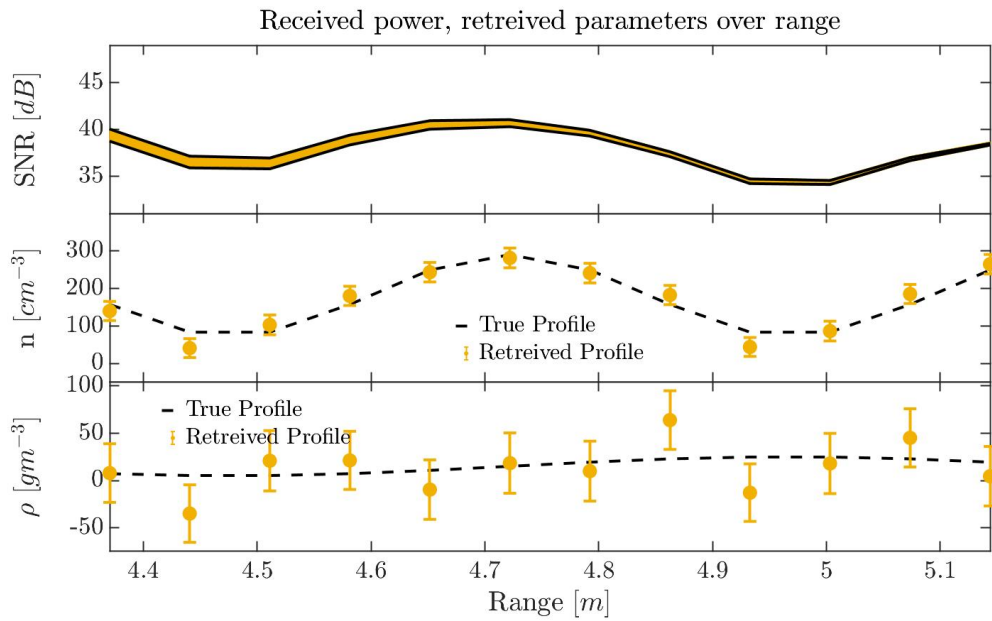


Figure 5.7: A comparison between the true and retrieved particle and water vapor concentration profiles, this with an integration time of 100 sec. At this integration time the particle measurements are becoming accurate and the humidity measurements are still not enough for room humidity but can be comparable to that needed in a process reactor. The SNR is also shown over range for all the different frequencies.

6

Conclusion

This chapter concludes the thesis with a summary of the findings and their implications, later discussing the needed future work and the general outlook of differential absorption spectroscopy using sub-millimeter wave radar.

6.1 Fixed target experiments

The experiments using a fixed target showed that it was difficult to use and other effects seemed to dominate over the absorption by water vapor. It is further not especially applicable in the power reactor, possibly at higher heights where there's no particles but rather only vapor, one could imagine using the wall as a fixed target and measuring the water vapor using several radars or spectrometers.

However one of driving forces behind using a sub-millimeter wave radar is range resolution and penetration in the particulate environment, both two things not needed in that use case. Therefore this mode of operation can be put aside.

6.2 Retrieval method: Formulation, experiments and simulations

In the thesis a retrieval method was synthesised and tested using a basic simulation technique, showing that for long integration times (≈ 100 s) it is possible to measure humidity at near room humidity conditions. However even at as low of an integration time as 10s the uncertainty is somewhat acceptable for very large concentrations of water vapor, meaning with optimization perhaps an integration time of 10s is feasible.

Rudimentary experiments shown in section 5.2 showed that the retrieval method that was synthesized in section 4.2 could extract a reasonable estimate of the particle concentration in the falling column of particles, showing that the underlying idea of measuring range dependent concentrations from their extinction is possible with the given hardware. While the poor results from water vapor retrievals are perhaps explained from the model not being accurate enough, perhaps this can be resolved from measuring a stronger absorption response from having a courser range resolution (larger ΔR) and higher concentrations of water vapor. A strengthening argument to this is that the work by NASA [6] has a bias on the order of 1 g m^{-3} at a resolution of $\Delta R = 20 \text{ m}$, while this work has a considerably higher resolution of $\Delta R = 15 \text{ cm}$. This would mean the same error in optical depth $T =$

$\Delta R \cdot \rho \cdot \sigma$ would yield a $\frac{20\text{m}}{0.15\text{m}} = 133$ times higher bias in humidity, which shows that the results of this thesis are at-least comparable to state of the art.

6.3 Future work

To continue work on the evaluation of the retrieval method synthesized in section 4.2, a more thorough approach should be taken. The different aspects of the experiment are below discussed one by one.

6.3.1 Particles

For future experiments the particle size distribution should be well known and taken into account in the calculation of the cross sections, the choice of particles should be done so that the extinction and back-scatter crosssection do not vary significantly within the distribution. This since it cannot be guaranteed that the size distribution wont be spatially varying in the experimental setup, thus causing uncertainty in the extinction crosssection and therefore the estimated concentration.

6.3.2 Water vapor concentration

The humidity levels should be significantly higher than normal atmospheric humidity levels, preferably several hundreds of grams. Although it should be noted that for very high concentrations of water vapor the line-width and thus absorption spectrum of water vapor will change as the partial pressure of water vapor is significantly increased with more humidity, this can be seen in section 2.3. Something that should be avoided for initial tests, but could be solved with a more advanced retrieval method.

6.3.3 Reference measurements

During the experiments using falling particles in this thesis the humidity has been controlled and measured but not the spatial profile of the particle concentration, this should be solved for future tests. A rudimentary measurement of the particle concentration should be used, perhaps a cloud of particles with a known mass inside. This would allow for integrating the retrieved particle concentration vector and multiply with the area of the setup(assuming it is a box) to estimate the total mass for comparison.

6.3.4 Experimental setup

For future experiments a fluidized bed should be used, as it allows for constant particles to be in the path of the beam. Without large amounts of pulsing as pouring in a stable manner is difficult, further it allows for practically indefinite measurements. It should also create a distribution of particles that vary with height, thus allowing one to not only compare the average particle concentration but also the profile retrieved.

6.3.5 Retrieval method

The retrieval method used in this thesis should be used for future evaluation, except in the case of a very large amount of water vapor. If the water vapor concentration is high enough that the partial pressure of water vapor is becoming a significant part of the pressure, then the absorption spectrum will change somewhat(see section 2.3). To allow for these type of measurements a non-linear retrieval method should be used, which could be solved with something like the Levenberg-Marquardt algorithm [16, Ch. 5]. The method for estimating the uncertainty of the retrieved profiles is also in need of a change if a non-linear retrieval method is used, a suggestions would be to see if using a linearization of the forward model around the estimated values is sufficient [16, Ch. 5].

Further the noise floor of the radar should be better characterized to take into account different noise levels for different range and frequency values.

6.3.6 Integration method

One of the difficulties of the experiments with falling particles was the corruption of a portion of the frequency bands, caused by a glitch that occurred regularly at a certain time in fast time. This error could mitigated to allow those frequency bands to also be used, this to gain more useful data. The major cause of long integration times is however the fact that the radar measures an equal amount on all sub-bands, which is not optimal. Ignoring the extinction by particles, the optimal integration scheme would be half on the maximum absorption and half at the minimum, to create the maximal contrast. Future work would include computationally solving the optimal three(or more) frequency sub-bands that yield the minimal estimated uncertainty of the water vapor profile, this at the sacrifice of the particle concentration.

6. Conclusion

References

- [1] *The Chalmers Power Central | Chalmers*. [Online]. Available: <https://www.chalmers.se/en/researchinfrastructure/cpp/Pages/default.aspx> (visited on 10/13/2021).
- [2] U. Platt and J. Stutz, *Differential optical absorption spectroscopy: principles and applications*, ser. Physics of Earth and space environments. Berlin: Springer, 2008, ISBN: 9783540211938 9783540757764.
- [3] K. B. Cooper, R. Roy, J. V. Siles, M. Lebsock, L. Millan, O. Pradhan, and R. R. Monje, “Differential absorption radar at 170 and 560 GHz for humidity remote sensing,” in *Passive and Active Millimeter-Wave Imaging XXIII*, D. A. Robertson and D. A. Wikner, Eds., Online Only, United States: SPIE, Apr. 2020, p. 1, ISBN: 9781510635999 9781510636002. DOI: 10.1117/12.2557138. [Online]. Available: <https://www.spiedigitallibrary.org/conference-proceedings-of-spie/11411/2557138/Differential-absorption-radar-at-170-and-560-GHz-for-humidity/10.1117/12.2557138.full> (visited on 09/27/2020).
- [4] R. J. Roy, M. Lebsock, L. Millán, R. Dengler, R. Rodriguez Monje, J. V. Siles, and K. B. Cooper, “Boundary-layer water vapor profiling using differential absorption radar,” English, *Atmospheric Measurement Techniques*, vol. 11, no. 12, pp. 6511–6523, Dec. 2018, ISSN: 1867-1381. DOI: <https://doi.org/10.5194/amt-11-6511-2018>. [Online]. Available: <https://amt.copernicus.org/articles/11/6511/2018/> (visited on 09/27/2020).
- [5] A. Battaglia, C. D. Westbrook, S. Kneifel, P. Kollias, N. Humpage, U. Löhnert, J. Tyynelä, and G. W. Petty, “G band atmospheric radars: New frontiers in cloud physics,” en, *Atmospheric Measurement Techniques*, vol. 7, no. 6, pp. 1527–1546, Jun. 2014, ISSN: 1867-8548. DOI: 10.5194/amt-7-1527-2014. [Online]. Available: <https://amt.copernicus.org/articles/7/1527/2014/> (visited on 09/27/2020).
- [6] R. J. Roy, M. Lebsock, L. Millán, and K. B. Cooper, “Validation of a G-Band Differential Absorption Cloud Radar for Humidity Remote Sensing,” en, *Journal of Atmospheric and Oceanic Technology*, vol. 37, no. 6, pp. 1085–1102, Jun. 2020, ISSN: 0739-0572. DOI: 10.1175/JTECH-D-19-0122.1. [Online]. Available: <https://journals.ametsoc.org/jtech/article/37/6/1085/345955/Validation-of-a-G-Band-Differential-Absorption> (visited on 09/21/2020).
- [7] L. Millán, M. Lebsock, N. Livesey, and S. Tanelli, “Differential absorption radar techniques: Water vapor retrievals,” en, *Atmospheric Measurement Techniques*, vol. 9, no. 6, pp. 2633–2646, Jun. 2016, ISSN: 1867-8548. DOI: 10.5194/amt-9-2633-

2016. [Online]. Available: <https://amt.copernicus.org/articles/9/2633/2016/> (visited on 09/19/2020).
- [8] M. I. Skolnik, Ed., *Radar handbook*, 3rd ed. New York: McGraw-Hill, 2008, OCLC: 185095728, ISBN: 9780071485470.
- [9] *Fluctuation Loss - Radartutorial*, en. [Online]. Available: <https://www.radartutorial.eu/01.basics/Fluctuation%20Loss.en.html,%20https://www.radartutorial.eu/01.basics/Fluctuation%20Loss.en.html> (visited on 10/12/2021).
- [10] *Pulse Integration - Radartutorial*, en. [Online]. Available: <https://www.radartutorial.eu/10.processing/Pulse%20Integration.en.html> (visited on 10/12/2021).
- [11] C. F. Bohren and D. R. Huffman, *Absorption and scattering of light by small particles*, eng. Weinheim: Wiley-VCH, 2004, OCLC: 254937169, ISBN: 9780471293408 9780471057727 9783527618156.
- [12] C. Mätzler, *MATLAB Functions for Mie Scattering and Absorption*. [Online]. Available: <https://omlc.org/software/mie/maetzlermie/Maetzler2002.pdf>.
- [13] L. Rothman, I. Gordon, Y. Babikov, A. Barbe, D. Chris Benner, P. Bernath, M. Birk, L. Bizzocchi, V. Boudon, L. Brown, A. Campargue, K. Chance, E. Cohen, L. Coudert, V. Devi, B. Drouin, A. Fayt, J.-M. Flaud, R. Gamache, J. Harrison, J.-M. Hartmann, C. Hill, J. Hodges, D. Jacquemart, A. Jolly, J. Lamouroux, R. Le Roy, G. Li, D. Long, O. Lyulin, C. Mackie, S. Massie, S. Mikhailenko, H. Müller, O. Naumenko, A. Nikitin, J. Orphal, V. Perevalov, A. Perrin, E. Polovtseva, C. Richard, M. Smith, E. Starikova, K. Sung, S. Tashkun, J. Tennyson, G. Toon, V. Tyuterev, and G. Wagner, "The HITRAN2012 molecular spectroscopic database," en, *Journal of Quantitative Spectroscopy and Radiative Transfer*, vol. 130, pp. 4–50, Nov. 2013, ISSN: 00224073. DOI: 10.1016/j.jqsrt.2013.07.002. [Online]. Available: <https://linkinghub.elsevier.com/retrieve/pii/S0022407313002859> (visited on 01/29/2021).
- [14] *Definitions and Units: Line-by-line Parameters*. [Online]. Available: <https://hitran.org/docs/definitions-and-units/>.
- [15] *Miscellaneous Dielectric Constants*. [Online]. Available: <https://www.microwaves101.com/encyclopedias/miscellaneous-dielectric-constants>.
- [16] C. D. Rodgers, *Inverse methods for atmospheric sounding: theory and practice*, eng, Reprinted, ser. Series on atmospheric oceanic and planetary physics 2. Singapore: World Scientific, 2004, OCLC: 254137862, ISBN: 9789810227401.
- [17] S. J. Orfanidis, *Electromagnetic Waves and Antennas*. [Online]. Available: <http://eceweb1.rutgers.edu/~orfanidi/ewa/> (visited on 09/20/2020).

A

Appendices

A.1 Noise model for retrieval method

The noise model is contained in the co-variance matrices S_y and S_b , which contain the noise for the vectors y and b respectively. Starting with S_y which originates from the uncertainty in the power measurements from each distance and frequency, and the co-variance in-between them, which is caused by windowing making adjacent range indices partially correlated. The model for the variance and co-variance is as seen in [6], however the co-variance model is assumed to contain a minor error, the dropping of N_{ind} . This is assumed to be the correct equation as the paper states that the equations should be the same however with average quantities and scaled by a factor decided to the window used, which is a Hamming window both in the case of this thesis and [6].

The variance and co-variance models used are seen in Equation A.1 and Equation A.2 respectively. These equations contain the signal to noise ratio for a certain range and frequency: $SNR^{i,j}$, to describe the Gaussian white noise of the receiver chain. Further they contain the number of statistically independent samples N_{ind} of the Swirling target that have been averaged in the incoherent integration stage in the signal processing, this describes the random fluctuations of the received power from a Swerling target as described in subsection 2.1.3. It can be seen that the variance of the received power of certain range and frequency only depends on itself, the SNR and the number of independent samples. The co-variance however is scaled by a factor and depends on the average power and SNR of a certain range index i and the adjacent indices $i \pm 1$. The number of independent samples is assumed to be equal to the number of pulses/sweeps that have been integrated, which depends on the integration time and the pulses per second which is reflected in the $\frac{N_{ind}}{T_{int}}$ number seen in subsection 4.2.2.

$$VAR[P^{i,j}] = \frac{(P^{i,j})^2}{N_{ind}} \cdot \left(1 + \frac{2}{(SNR^{i,j})} + \frac{2}{(SNR^{i,j})^2}\right) \quad (A.1)$$

$$COV[P^{i,j}, P^{i\pm 1,j}] = \frac{(P^{i,j} + P^{i\pm 1,j})^2}{9N_{ind}} \cdot \left(1 + \frac{4}{(SNR^{i,j} + SNR^{i\pm 1,j})} + \frac{8}{(SNR^{i,j} + SNR^{i\pm 1,j})^2}\right) \quad (A.2)$$

Now a co-variance matrix for the received power can be made: S_P and then together with a first order Taylor expansion of $y = \ln(P)$ a co-variance matrix for y can be obtained S_y . The matrix is tri-diagonal, with the diagonal representing independent noise and the

lower and upper diagonal representing correlated noise between adjacent range indices. The co-variance matrices for each frequency are on the form in Equation A.4, which contains the variance and co-variance seen in Equation A.1, A.2 and the Kronecker delta $\delta^{j,k}$ which is defined in Equation A.3. These co-variance matrices are then put together as the diagonal of a larger $(N_f \cdot N_r) \times (N_f \cdot N_r)$ matrix to form the full co-variance matrix as seen in Equation A.5 [6]. Since $y = \ln(P)$ it needs to be linearized to estimate the uncertainty of y using the uncertainty of P , this is done using the Jacobian of y with respect to P , J_P [6]. Then the co-variance matrix of P can be used to calculate the co-variance matrix for y using $S_y = J_P S_P J_P^T$ [6], since this is based on a first order Taylor expansion it will not be applicable for extreme amounts of noise.

$$\delta^{j,k} = \begin{cases} 1, & \text{for } j = k \\ 0, & \text{for } j \neq k \end{cases} \quad (\text{A.3})$$

$$[S_P(f_i)]^{j,k} = \text{VAR}[P^{j,i}] \delta^{j,k} + \text{COV}[P^{j,i}, P^{j\pm 1,i}] (\delta^{j,k+1} + \delta^{j,k-1}) \quad (\text{A.4})$$

$$S_{P_r} = \text{DIAG}[S_P(f_1), S_P(f_2), \dots, S_P(f_{N_f})] \quad (\text{A.5})$$

A.2 Code used for simulations

This code was used for simulations, but is also able to read real data and process it.

```

1 % some testing using retrieval method - 25 frequency pt
2 clc
3 clear all
4 format shorteng
5
6 C0 = 299792458; % m/s
7 eps0 = 8.8541878128E-12; % F/m
8 my0 = 1.25663706212E-6; %H/m
9
10 %To allow for fancy colorschemes
11 addpath('/Users/z3bb0/Documents/MATLAB/Matplotlib')
12
13 %mie code
14 addpath('Mie-Matlab-Maetzler-v2')
15
16 C_1 = '#0000FF'%blue
17 C_1_RGBTRIPLET = [0, 0, 255]/255;
18 C_2 = '#F2B000'%Amber
19 C_2_RGBTRIPLET = [242, 176, 0]/255;
20 W_line_1 = 4
21 S_marker_1 = 35
22 S_font_1 = 35
23 S_marker_2 = 55
24
25 fake = true%true means fake data is used(simulations), false means data is read
26 filename_radardata = '/Users/z3bb0/Documents/GitHub/EXJOB-19May2021/↔
    Nf_Nr_10subbands_fix'
27 %filename_radardata = '/Users/z3bb0/Documents/GitHub/EXJOB-17May2021/↔
    Nf_Nr_10subbands_700Nint_fix'
28 filename_radardata = '/Users/z3bb0/Documents/GitHub/EXJOB-24May2021/↔
    Nf_Nr_1000MHz_10subband_fixed'
29 %filename_radardata = '/Users/z3bb0/Documents/GitHub/EXJOB-26May2021/↔
    Nf_Nr_1000MHz_15subband_SG2_fixed'
30 %filename_radardata = '/Users/z3bb0/Documents/GitHub/EXJOB-26May2021/↔
    Nf_Nr_1000MHz_15subband_TB1_fixed'
31 filename_radardata = '/Users/z3bb0/Documents/GitHub/EXJOB-2021-05-27/↔
    Nf_Nr_1000MHz_15subband_SG2_fixed'%this flow rate(higher) seems ok
32 filename_radardata = '/Users/z3bb0/Documents/GitHub/EXJOB-31May2021/↔
    Nf_Nr_15subband_128pulser_largeFlow_fixed'
33 %filename_radardata = '/Users/z3bb0/Documents/GitHub/EXJOB-31May2021/↔
    Nf_Nr_15subband_128pulser_bronze_fixed'
34
35 %make some fake data into a file, disabled
36 print = false;
37
38 %plot raw data
39 plotting = false
40
41 %For non fake data only, start and stop indices for integration in slow
42 %time
43 i_integration_start = 32
44 i_integration_stop = i_integration_start + 0
45
46 %Range indices to start/stop at
47 i_R_stop = 18
48 i_R_start = 5
49
50
51 %This method assumes a single particle size or to the very least
52 %homogenous distribution can be used to describe it
53
54 %It extracts particles, humidity and calibration
55
56

```


A. Appendices

```
188 %Assemble the forward model and generate the fake received power, then
189 %add noise
190
191
192 x_actual = [k_r ; n ; rho];
193 %y = log([P(f1, all r) ; .. ; P(fN_f, all r)])
194
195 else
196 %data is not fake! Read real data
197 addpath('/Users/z3bb0/Documents/GitHub/EXJOB-Data')
198
199 delim = '\t';
200 %fid = fopen(filename,'w')
201 %A = readmatrix(filename,'FileType','text','Delimiter',delim);
202 A = dlmread(filename_radardata,delim,0,0);
203 A_size = size(A)
204 %Read frequencies
205 %f = rmmissing(A(1,:));
206 %N_f = length(f);
207 N_f = A(1,1)
208 N_r = A(1,2)
209 N_T = A(1,3)
210 dR = A(1,4)
211 dT = 30e-6
212 disp('dT is not read, use 1 sec')
213 disp('F-vector not read, guessing')
214 disp('R-vector not read, guessing')
215 r = 2.5 + (0:N_r-1)*dR;
216
217 r = r.';
218 f = f.';
219
220 i_r_start = 1;
221 i_r_end = N_r;
222 r = r(i_r_start:i_r_end);
223 N_r = length(r);
224
225
226
227 %Read ranges
228 %r = rmmissing(A(2,:));
229 %N_r = length(r);
230 %dR = r(2)-r(1);
231
232 %Read slow time
233 %T = rmmissing(A(3,:));
234 %N_T = length(T);
235 %dT = T(2)-T(1);
236
237 %Read power matrix
238 N_slowtime_int = i_integration_stop + 1 - i_integration_start;
239 %Pr_matrix = 10.^(A(2:end,:)/10);
240 %Pr_matrix = Pr_matrix(1:N_f, 1:N_r);
241
242 Pr_matrix = zeros(N_f, N_r);
243 %for i = 0:N_slowtime_int-1
244 for i = i_integration_start:i_integration_stop
245 %Integrate power
246 %Pr_matrix = Pr_matrix + 10.^(A(2 + i*N_f:1+N_f + i*N_f,1:N_r)/10)/↔
    N_slowtime_int;%dB version
247 Pr_matrix = Pr_matrix + A(2 + i*N_f:1+N_f + i*N_f,1:N_r)/N_slowtime_int;%↔
    linear version
248 end
249
250 Pr_matrix = Pr_matrix.%;%transpose it
251 disp('Data is in dB already, convert to linscale then follow along as usual')
252
253 Pn_dB = -70;%Noise floor power
254 %N_independent = 1e3%number of independent per slow time sample
255 N_independent = round(dT*N_slowtime_int/100e-6);%assuming 100uS gives 1 ↔
```

```

independent
256 N_independent = N_slowtime_int*2048;
257 %N_independent = 2048;
258 %N_independent = 100e3;
259
260 %remove frequency band in middle 5,6,7,8
261 i_skip = 5;
262 N_f = N_f-1;
263 Pr_matrix = Pr_matrix(:, [1:i_skip-1, i_skip+1:end], :);
264 f = f([1:i_skip-1, i_skip+1:end]);
265
266 i_skip = 5;
267 N_f = N_f-1;
268 Pr_matrix = Pr_matrix(:, [1:i_skip-1, i_skip+1:end], :);
269 f = f([1:i_skip-1, i_skip+1:end]);
270
271 i_skip = 5;
272 N_f = N_f-1;
273 Pr_matrix = Pr_matrix(:, [1:i_skip-1, i_skip+1:end], :);
274 f = f([1:i_skip-1, i_skip+1:end]);
275
276 i_skip = 5;
277 N_f = N_f-1;
278 Pr_matrix = Pr_matrix(:, [1:i_skip-1, i_skip+1:end], :);
279 f = f([1:i_skip-1, i_skip+1:end]);
280
281
282 %remove lowest, highest freq
283 N_skip = 1
284 N_f = N_f-N_skip*2;
285 Pr_matrix = Pr_matrix(:,1+N_skip:end-N_skip);
286 f = f(1+N_skip:end-N_skip);
287 sigma_ext = sigma_ext(1+N_skip:end-N_skip);
288 sigma_b = sigma_b(1+N_skip:end-N_skip);
289 sigma_h2o = sigma_h2o(1+N_skip:end-N_skip);
290 k_f = k_f(1+N_skip:end-N_skip);
291 %fclose(fid);
292
293 %remove some ranges
294 Pr_matrix = Pr_matrix(i_R_start:i_R_stop,:);
295 r = r(i_R_start:i_R_stop);
296 N_r = length(r);
297
298 end
299
300
301 T_fakedata = toc;
302 tic
303 %Add together identity matrix and dust
304 disp('Removing power dependency on dust concentration to avoid non linear ↔
treatment, only seen in extinction (TBD, this is why its weird)')
305 disp('Change from particles per m^3 to million per m^3 = per cm^3')
306 I = [diag(ones(1, N_r))];
307 T_ext = [- sigma_ext(1)*dR*2*1E6 * tril(ones(N_r, N_r))];
308 T_H2O = [-sigma_h2o(1)*dR*2 * tril(ones(N_r, N_r))];
309 for i = 2:N_f
310 %I = [I ; [ diag(ones(1, N_r)) , diag(ones(1, N_r)) - sigma_ext(i)*dR*2 * tril(↔
(ones(N_r, N_r))] ];
311 I = [I ; diag(ones(1, N_r))];
312 T_ext = [T_ext ; - sigma_ext(i)*dR*2*1E6 * tril(ones(N_r, N_r))];
313 T_H2O = [T_H2O ; -sigma_h2o(i)*dR*2 * tril(ones(N_r, N_r))];
314 end
315
316 % %Make forward model
317 % %Add together T matrix for all frequencies
318 % T = [-sigma_h2o(1)*dR*2 * tril(ones(N_r, N_r))];
319 % for i = 2:N_f
320 % T = [T ; -sigma_h2o(i)*dR*2 * tril(ones(N_r, N_r))];
321 % end
322

```



```

392 %Fake data is now assembled
393 %Pr_matrix is data
394 %r is range
395 %f is frequency
396 %x
397
398
399 end
400
401 %Make a noise model that includes SNR, Swirling target distribution
402 disp('Further assume Hamming window as in VIPR paper, cite that here too')
403
404
405 disp('This noise model is slightly simplified but completely from VIPR paper')
406 tic
407 %Make buffer
408 Sy_lin = zeros(N_r*N_f, N_r*N_f);%remove?
409
410 for i = 1:N_f
411 %Make noise model for each frequency point, automatically adds onto
412 %buffer
413
414 %SNR for each range for this frequency
415 SNR_r = Pr_matrix(:,i)/10^(Pn_dB/10);
416
417 %Self variance to describe noise
418 var_Pr_self = Pr_matrix(:,i).^2./N_independent.*( 1 + 2./SNR_r + 2./SNR_r.^2)↵
419 ;
420 Sy_lin = Sy_lin + diag([zeros(N_r*(i-1), 1) ; k_f(i)^2 .*var_Pr_self ; zeros(↵
421 N_r*(N_f-i), 1)], 0);
422
423 %Covariance between adjacent range bins from windowing
424
425 %Calculate the mean power at r +/- dR, Both are this r + lower/upper
426 P_mean_lower = Pr_matrix(2:end,i)/2 + Pr_matrix(1:end-1,i)/2;
427 P_mean_upper = Pr_matrix(1:end-1,i)/2 + Pr_matrix(2:end,i)/2;
428
429 %Assume uniform noise floor Pn_dB [dB] noise everywhere
430 Pn = 10.^(Pn_dB/10);%to linear scale
431
432 %Calculate mean SNR between ranges, assuming constant noise(in R, maybe
433 %modify for frequency)
434 SNR_mean_lower = P_mean_lower ./ Pn;
435 SNR_mean_upper = P_mean_upper ./ Pn;
436
437 %Calculate the Covariance between r, +/- dR, assuming Hanning window
438 cov_Pr_lower = 4/9*P_mean_lower.^2 .* ( 1 + 2./SNR_mean_lower + 2./↵
439 SNR_mean_lower.^2 );
440 cov_Pr_upper = 4/9*P_mean_upper.^2 .* ( 1 + 2./SNR_mean_upper + 2./↵
441 SNR_mean_upper.^2 );
442
443 %Make the lower, upper diagonal matrices and add to Sy
444
445 %disp('No off diagonal elements in Sy_lin, Sy')
446 %Make exception for first, last sample
447 if i == 1
448 %Skip first zeros as it breaks for off diagonal
449
450 Sy_lin = Sy_lin + diag([ k_f(i).^2 .*cov_Pr_lower ; zeros((N_r)*(N_f-i), ↵
451 1)], -1);
452 Sy_lin = Sy_lin + diag([ k_f(i).^2 .* cov_Pr_upper ; zeros((N_r)*(N_f-i), ↵
453 1)], 1);
454 elseif i == N_f
455 %Breaks for last, skip that zero matrix
456 Sy_lin = Sy_lin + diag([zeros((N_r)*(i-1), 1) ; k_f(i).^2 .* cov_Pr_lower↵
457 ], -1);
458 Sy_lin = Sy_lin + diag([zeros((N_r)*(i-1), 1) ; k_f(i).^2 .* cov_Pr_upper↵
459 ], 1);
460 else
461 %Not first/ last index, just use normal equation

```

A. Appendices

```
454     Sy_lin = Sy_lin + diag([zeros((N_r)*(i-1), 1) ; k_f(i).^2 .* ←
455         cov_Pr_lower ; zeros((N_r)*(N_f-i), 1)], -1);
456     Sy_lin = Sy_lin + diag([zeros((N_r)*(i-1), 1) ; k_f(i).^2 .* ←
457         cov_Pr_upper ; zeros((N_r)*(N_f-i), 1)], 1);
458
459     end
460
461 end
462
463 disp('Assume 1/N_indep is missing from off diagonal elements...Test fix')
464 Sy_lin = Sy_lin ./ N_independent;
465 for i = 1:size(Sy_lin,1)
466     %step through and multiply by N to cancel double divide
467     Sy_lin(i,i) = Sy_lin(i,i)*N_independent;
468 end
469
470
471 %Taylor expand y = ln(z) to obtain the Jacobian
472 %y = ln(z), dy/dz = 1/z for each index
473 y = log( Pr_matrix(:,1) * k_f(1) );
474 for i = 2:N_f
475     %assemble z = Pr * r^2 * K_f(f)
476     y = [y ; log( Pr_matrix(:,i) * k_f(i) )];
477 end
478
479 y_lin = exp(y);
480
481 Jy_lin = diag(1./(y_lin));
482
483 %Use Jacobian to calculate Covariance matrix of y:
484 Sy = Jy_lin * Sy_lin * Jy_lin.';
485
486 T_noisemodel = toc;
487
488
489 if fake == true
490     %Add noise using covariance matrix noise model
491     noise = normrnd(0, 1, N_r*N_f, 1);
492     noise = chol(Sy, 'lower') * noise;
493     y_old = y;
494     y = y + noise;
495
496     %Convert to how radar saves data, in linear form
497     y_linear = exp(y);
498     Pr_matrix = y_linear(1:N_r);
499     for i = 2:N_f
500         i_low = (i-1)*N_r + 1;
501         i_high = i*N_r;
502         %size(y(i_low:i_high))
503         Pr_matrix = [Pr_matrix , y_linear(i_low:i_high)];
504     end
505 end
506
507 if plotting == true
508     %plot raw data
509     figure('Renderer', 'painters', 'Position', [10 10 1600 1100])
510     plot(r,10*log10(Pr_matrix))
511 end
512
513 %start of algorithm, it's the same for both fake and real data
514
515 % %Plot received power
516 % figure('Renderer', 'painters', 'Position', [10 10 1600 1100])
517 % subplot(2,1,1)
518 % plot(r,10*log10(Pr_matrix), 'LineWidth',4)
519 % hold on
520 % plot([min(r) max(r)], [1 1]*Pn_dB, '--b', 'LineWidth',4)
521 % xlabel('Range [m]')
```

```

522 % ylabel('Pr [dB]')
523 % title('Received power for all bands, over range')
524 % set(gca,'fontsize',18)
525 % grid on
526 %
527 % subplot(2,1,2)
528 % plot(f*1E-9,10*log10(Pr_matrix'), 'LineWidth',4)
529 % hold on
530 % plot([min(f) max(f)]*1E-9,[1 1]*Pn_dB,'--b', 'LineWidth',4)
531 % xlabel('Frequency [GHz]')
532 % ylabel('Pr [dB]')
533 % title('Received power for all ranges, over frequency')
534 % set(gca,'fontsize',18)
535 % grid on
536 % xlim([min(f) max(f)]*1E-9)
537 %
538 %
539 % %Plot received power but with picture color format
540 % figure('Renderer', 'painters', 'Position', [10 10 1600 1100])
541 % [%X,Y] = meshgrid(f,r);
542 % %contour(X,Y,Pr_matrix)
543 % imagesc(f*1E-9,r,10*log10(Pr_matrix));
544 % N_axis = 10;
545 % xticks(1E-9 * linspace(min(f), max(f), N_axis));
546 % yticks( linspace(min(r), max(r), N_axis) );
547 % colormap('viridis')
548 % cbar = colorbar;
549 % cbar.Title.String = 'P_{received}'
550 %
551 % ylabel('Range [m]')
552 % xlabel('Frequency [GHz]')
553 % zlabel('?')
554 % title('Received power [dB]')
555 % set(gca,'fontsize',18)
556 %
557 tic
558 %
559 %Assemble y
560 y_lin = Pr_matrix(:,1) ./ k_f(1);%log(Pr)
561 for i = 2:N_f
562     %Make z
563     y_lin = [y_lin ; Pr_matrix(:,i) ./ k_f(i)];
564 end
565 %
566 y = log(y_lin);
567 %
568 %
569 disp('Add uncertainty of b')
570 Se = diag([ones(1,N_r*N_f)] * 0; % S_e = J_b * S_b * J_b^T, uncertainty in B is ←
    sigma_d^2/d for VIPR)
571 %
572 %Invert y = Ax, using measured data to estimate x, x_hat
573 x_hat = inv(A.' * inv(Sy + Se) * A) * A.' * inv(Sy + Se) * (y-b);
574 k_r_hat = x_hat(1:N_r);
575 n_hat = x_hat(N_r+1:2*N_r);
576 rho_hat = x_hat(2*N_r+1:end);
577 %
578 lambda_reg = 0;%not implemented yet add + lambda_reg.*A in inversion
579 Sx_hat = inv( A.' *inv(Sy + Se) * A);%estimated covariance matrix of retrieved ←
    state variables
580 Sx_hat_diag = diag(Sx_hat,0);
581 sigma_n_hat = sqrt(Sx_hat_diag(N_r+1:2*N_r));
582 sigma_rho_hat = sqrt(Sx_hat_diag(2*N_r+1:end));
583 %
584 T_inversion = toc;
585 %
586 %
587 %Calculate the mean over range for the concentration, useful for getting
588 %something out of lower integration times
589 %

```

A. Appendices

```
590 %Done using the var^-1 = std^-2 as weight for each value of rho_hat, this assumes↔
      to
591 %correlations which is not true
592 disp('Mean rho does not take into account the correlations between ranges, to be ↔
      changed!')
593 w = 1./ ( sigma_n_hat.^2 );
594 %remove 1st, last sample in mean
595 w(1) = 0;
596 w(end) = 0;
597 w = w / sum( w );%normalize
598 n_mean_hat = sum( n_hat .* w );
599 sigma_n_mean_hat = sqrt( sum( w.^2 .* sigma_n_hat.^2 ) );
600
601
602 %Calculate the mean over range for the water vapor, useful for getting
603 %something out of lower integration times
604
605 %Done using the var^-1 = std^-2 as weight for each value of rho_hat, this assumes↔
      to
606 %correlations which is not true
607 disp('Mean rho does not take into account the correlations between ranges, to be ↔
      changed!')
608 w = 1./ ( sigma_rho_hat.^2 );
609 %remove 1st, last sample in mean
610 w(1) = 0;
611 w(end) = 0;
612 w = w / sum( w );%normalize
613 rho_mean_hat = sum( rho_hat .* w );
614 sigma_rho_mean_hat = sqrt( sum( w.^2 .* sigma_rho_hat.^2 ) );
615
616 disp(' ')
617 disp(['Mean retrieved humidity is: ', sprintf('%3.5g', rho_mean_hat), ' +- ', ↔
      sprintf('%0.2g', sigma_rho_mean_hat), ' [g/cm^3]'])
618 if fake == true
619     %Print actual humidity
620     disp(['Mean actual humidity is: ', sprintf('%3.5g', mean(rho)), ' [g/cm^3]', ↔
          ', the relative uncertainty is: ', sprintf('%1.3g',100* sigma_rho_mean_hat↔
          /mean(rho)), ' [%]'])
621 end
622
623 %See wikipedia page weighted mean, under accounting for correlations! For
624 %using COV....
625 %J = ones(N_r, 1);
626
627
628 %Plot data and fake data for comparison
629 if fake == true
630     %plot data but with real values for comparison
631     figure('Renderer', 'painters', 'Position', [10 10 1600 1100])
632     subplot(3,1,1)
633     % plot(r, k_r + log(n), '--', 'LineWidth', W_line_1, 'Color', C_1)
634     % hold on
635     % plot(r, k_r_hat, '.', 'MarkerSize', S_marker_1, 'Color', C_2)
636     % xlabel('Range [m]')
637     % ylabel('Range calfactor + ln(n)')
638     % set(gca,'fontsize',S_font_1)
639     % legend('boxoff')
640     % legend('Test data', 'Retrieved','Location', 'Best')
641     % grid on
642     % xlim([min(r)+dR max(r)-dR])
643
644     %Plot with black line for frequencies: 1, N_f
645     plot(r,10*log10(Pr_matrix(:,2:end-1)), 'LineWidth',4, 'Color', C_2)
646     hold on
647     plot(r,10*log10(Pr_matrix(:,1)), 'LineWidth',4, 'Color', 'black')
648     plot(r,10*log10(Pr_matrix(:,end)), 'LineWidth',4, 'Color', 'black')
649
650     plot([min(r) max(r)],[1 1]*Pn_dB, '--b', 'LineWidth',4, 'Color', C_2)
651     xlabel('Range [m]')
652     ylabel('Pr [dB]')
```

```

653 title('Received power for all bands, over range')
654 set(gca,'fontsize',S_font_1)
655 grid on
656 xlim([min(r), max(r)])
657
658
659
660 subplot(3,1,2)
661 plot(r, n, '--', 'LineWidth', W_line_1, 'Color', C_2)
662 hold on
663 %plot(r, n_hat, '.', 'MarkerSize', S_marker_1, 'Color', C_2)
664 errorbar(r,n_hat,sigma_n_hat, '.', 'MarkerSize', S_marker_2, 'Color', C_1)
665 xlabel('Range [m]')
666 ylabel('n [#/cm^3]')
667 set(gca,'fontsize',S_font_1)
668 legend('boxoff')
669 legend('Test data', 'Retrieved','Location', 'Best')
670 grid on
671 xlim([min(r)+dR max(r)-dR])
672 %yyaxis right
673 %ylabel('Particle concentration [g/m^3]')
674
675
676 subplot(3,1,3)
677 plot(r, rho, '--', 'LineWidth', W_line_1, 'Color', C_2)
678 hold on
679 %plot(r, rho_hat, '.', 'MarkerSize', S_marker_1, 'Color', C_2)
680 errorbar(r,rho_hat,sigma_rho_hat, '.', 'MarkerSize', S_marker_2, 'Color', C_1)
681
682 xlabel('Range [m]')
683 ylabel('\rho [g/m^3]')
684 set(gca,'fontsize',S_font_1)
685 legend('boxoff')
686 legend('Test data', 'Retrieved','Location', 'Best')
687 grid on
688 xlim([min(r)+dR max(r)-dR])
689
690
691
692
693
694 %fancy fake data plot...
695 figure('Renderer', 'painters', 'Position', [10 10 1600 1100])
696 resultplot_1_1 = subplot(3,1,1);
697 %Plot with black line for frequencies: 1, N_f
698 plot(r,10*log10(Pr_matrix(:,2:end-1))-Pn_dB, 'LineWidth',4, 'Color', C_2)
699 hold on
700 plot(r,10*log10(Pr_matrix(:,1))-Pn_dB, 'LineWidth',4, 'Color', 'black')
701 plot(r,10*log10(Pr_matrix(:,end))-Pn_dB, 'LineWidth',4, 'Color', 'black')
702
703 plot([min(r) max(r)], [1 1]*Pn_dB, '--b', 'LineWidth',4, 'Color', C_2)
704 %xlabel('Range, r [m]', 'interpreter', 'latex')
705 %ylabel('$P_r - P_n$ [dB]', 'interpreter', 'latex')
706 ylabel('SNR [dB]', 'interpreter', 'latex', 'Units', 'normalized', 'Position'←
, [-0.075 0.5])
707
708
709 title('Received power, retrieved parameters over range','interpreter', 'latex'←
)
710 set(gca,'fontsize', S_font_1)
711 %grid on
712 xlim([min(r), max(r)])
713 set(gca,'XTickLabel', []); %test
714 xlim([min(r)+dR max(r)-dR])
715 set(gca,'LineWidth', 2)
716 ylim([ 10*floor((min(10*log10(Pr_matrix), [], 'all')-1 - Pn_dB)/10)+1 , 10*ceil←
((max(10*log10(Pr_matrix), [], 'all')+1 - Pn_dB)/10)-1])
717 set(gca,'TickLabelInterpreter', 'latex')
718

```

```

719
720     resultplot_1_2 = subplot(3,1,2);
721     plot(r, n, '--', 'LineWidth', W_line_1, 'Color', 'black')
722     hold on
723     errorbar(r,n_hat,sigma_n_hat, '.', 'MarkerSize', S_marker_2, 'Color', C_2)
724     %xlabel('Range  $[m]$ ','$', 'interpreter','latex')
725     ylabel('n  $[cm^{-3}]$ ','$', 'interpreter','latex', 'Units', 'normalized','Position'↵
726         ', [-0.075 0.5])
727     set(gca, 'fontsize', S_font_1)
728     legend('boxoff')
729     legend('True Profile', 'Retreived Profile', 'Location', 'Best', 'interpreter', '↵
730         latex')
731
732     %grid on
733     %xlim([min(r)+dR max(r)-dR])
734     %yyaxis right
735     %ylabel('Particle concentration  $[g/m^3]$ ')
736     set(gca, 'XTickLabel', []); %test
737     xlim([min(r)+dR max(r)-dR])
738     set(gca, 'LineWidth', 2)
739     set(gca, 'TickLabelInterpreter', 'latex')
740     ylim([ 50*floor((min(n_hat(2:end-1)-sigma_n_hat(2:end-1), [], 'all')-1)/50)-49 ↵
741         , 50*ceil((max(n_hat(2:end-1)+sigma_n_hat(2:end-1), [], 'all')+1)/50)+49])
742
743     resultplot_1_3 = subplot(3,1,3);
744     plot(r, rho, '--', 'LineWidth', W_line_1, 'Color', 'black')
745     hold on
746
747     errorbar(r,rho_hat,sigma_rho_hat, '.', 'MarkerSize', S_marker_2, 'Color', C_2↵
748         )
749     xlabel('Range  $[m]$ ','$', 'interpreter','latex')
750     ylabel('$\rho$  $[g m^{-3}]$ ','$', 'interpreter','latex', 'Units', 'normalized','↵
751         Position', [-0.075 0.5])
752     set(gca, 'fontsize', S_font_1)
753     legend('boxoff')
754     legend('True Profile', 'Retreived Profile', 'Location', 'Best', 'interpreter', '↵
755         latex')
756
757     %grid on
758     xlim([min(r)+dR max(r)-dR])
759     set(gca, 'LineWidth', 2)
760     set(gca, 'TickLabelInterpreter', 'latex')
761     ylim([ 5*floor((min(rho_hat(2:end-1)-sigma_rho_hat(2:end-1), [], 'all')-1)/5)-4↵
762         , 5*ceil((max(rho_hat(2:end-1)+sigma_rho_hat(2:end-1), [], 'all')+1)/5)+4])
763
764     %Make them share x-axis
765     p1 = get(resultplot_1_1, 'Position');
766     p2 = get(resultplot_1_2, 'Position');
767     p3 = get(resultplot_1_3, 'Position');
768     p1(2) = p2(2)+p2(4);
769     p3(2) = p2(2)-p2(4);
770     set(resultplot_1_1, 'pos', p1);
771     set(resultplot_1_3, 'pos', p3);
772
773 end
774
775 %Plot data and mean humidity for comparison
776 %
777 if true
778     %plot data but with mean values for comparison
779     figure('Renderer', 'painters', 'Position', [10 10 1600 1100])
780     resultplot_1_1 = subplot(3,1,1);
781     %Plot with black line for frequencies: 1, N_f
782     plot(r, 10*log10(Pr_matrix(:,2:end-1))-Pn_dB, 'LineWidth', 4, 'Color', C_2)
783     hold on
784     plot(r, 10*log10(Pr_matrix(:,1))-Pn_dB, 'LineWidth', 4, 'Color', 'black')
785     plot(r, 10*log10(Pr_matrix(:,end))-Pn_dB, 'LineWidth', 4, 'Color', 'black')
786
787

```

```

882 plot([min(r) max(r)], [1 1]*Pn_dB, '--b', 'LineWidth', 4, 'Color', C_2)
883 xlabel('Range, r [m]', 'interpreter', 'latex')
884 ylabel('$P_r - P_n$ [dB]', 'interpreter', 'latex')
885 ylabel('SNR [dB]', 'interpreter', 'latex', 'Units', 'normalized', 'Position' ←
      , [-0.075 0.5])
886
887
888 title('Received power, retrieved parameters over range', 'interpreter', 'latex' ←
      )
889 set(gca, 'fontsize', S_font_1)
890 %grid on
891 xlim([min(r), max(r)])
892 set(gca, 'XTickLabel', []); %test
893 xlim([min(r)+dR max(r)-dR])
894 set(gca, 'LineWidth', 2)
895 ylim([-9, 10*ceil((max(10*log10(Pr_matrix), [], 'all')+1 - Pn_dB)/10)+9])
896 set(gca, 'TickLabelInterpreter', 'latex')
897
898
899 resultplot_1_2 = subplot(3,1,2);
900 %plot(r, n, '--', 'LineWidth', W_line_1, 'Color', C_2)
901 %hold on
902 %plot(r, n_hat, '.', 'MarkerSize', S_marker_1, 'Color', C_2)
903 r2 = [r', fliplr(r')];
904 inBetween = [ones(1, N_r)*(n_mean_hat-sigma_n_mean_hat), fliplr(ones(1, N_r) ←
      *(n_mean_hat+sigma_n_mean_hat))];
905 fill(r2, inBetween, C_2_RGBTRIPLET);
906 hold on
907 errorbar(r, n_hat, sigma_n_hat, '.', 'MarkerSize', S_marker_1, 'Color', C_1)
908 xlabel('Range [m]', 'interpreter', 'latex')
909 ylabel('n [cm-3]', 'interpreter', 'latex', 'Units', 'normalized', 'Position' ←
      , [-0.075 0.5])
910 set(gca, 'fontsize', S_font_1)
911 legend('boxoff')
912 %legend('Retrieved', 'Location', 'Best', 'interpreter', 'latex')
913 legend(['\langle n \rangle = ', sprintf('%3.5g', n_mean_hat), ' $\pm$ ', ←
      sprintf('%0.2g', sigma_n_mean_hat), ' $[cm^{-3}]$'], 'Retrieved', 'Location' ←
      , 'Best', 'interpreter', 'latex')
914 %\langle rho$ \rangle
915 %grid on
916 %xlim([min(r)+dR max(r)-dR])
917 %yyaxis right
918 %ylabel('Particle concentration [g/m3'])
919 set(gca, 'XTickLabel', []); %test
920 xlim([min(r)+dR max(r)-dR])
921 set(gca, 'LineWidth', 2)
922 set(gca, 'TickLabelInterpreter', 'latex')
923 ylim([50*floor((min(n_hat(2:end-1)-sigma_n_hat(2:end-1), [], 'all')-1)/50)-49 ←
      , 50*ceil((max(n_hat(2:end-1)+sigma_n_hat(2:end-1), [], 'all')+1)/50)+49])
924
925
926 resultplot_1_3 = subplot(3,1,3);
927 %plot(r, rho, '--', 'LineWidth', W_line_1, 'Color', C_1)
928 r2 = [r', fliplr(r')];
929 inBetween = [ones(1, N_r)*(rho_mean_hat-sigma_rho_mean_hat), fliplr(ones(1, ←
      N_r)*(rho_mean_hat+sigma_rho_mean_hat))];
930 fill(r2, inBetween, C_2_RGBTRIPLET);
931 hold on
932 %plot(r, rho_hat, '.', 'MarkerSize', S_marker_1, 'Color', C_2)
933 errorbar(r, rho_hat, sigma_rho_hat, '.', 'MarkerSize', S_marker_1, 'Color', C_1 ←
      )
934 xlabel('Range [m]', 'interpreter', 'latex')
935 ylabel('$\rho$ [g m-3]', 'interpreter', 'latex', 'Units', 'normalized', ' ←
      Position', [-0.075 0.5])
936 set(gca, 'fontsize', S_font_1)
937 legend('boxoff')
938 legend(['\langle \rho \rangle = ', sprintf('%3.5g', rho_mean_hat), ' $\pm$ ←
      ', sprintf('%0.2g', sigma_rho_mean_hat), ' $[gm^{-3}]$'], 'Retrieved', ' ←
      Location', 'Best', 'interpreter', 'latex')
939 %\langle rho$ \rangle

```

A. Appendices

```
840 %grid on
841 xlim([min(r)+dR max(r)-dR])
842 set(gca,'LineWidth',2)
843 set(gca,'TickLabelInterpreter','latex')
844 ylim([ 5*floor((min(rho_hat(2:end-1)-sigma_rho_hat(2:end-1),[],'all')-1)/5)-4↔
      , 5*ceil((max(rho_hat(2:end-1)+sigma_rho_hat(2:end-1),[],'all')+1)/5)+4])
845
846
847 %Make them share x-axis
848 p1 = get(resultplot_1_1, 'Position');
849 p2 = get(resultplot_1_2, 'Position');
850 p3 = get(resultplot_1_3, 'Position');
851 p1(2) = p2(2)+p2(4);
852 p3(2) = p2(2)-p2(4);
853 set(resultplot_1_1, 'pos', p1);
854 set(resultplot_1_3, 'pos', p3);
855
856 end
857
858
859
860 %Fix list for future
861 % -read real data
862 % -Plot real data without comparison with fake actual data
863 % -Investigate how to display covariance data better
864 % -Investigate if there's a mistake in the VIPR paper
865 % -Add to estimate K_f(f)
866 % -Add way to investigate fit? chi square test?
867
868
869
870
871
872
873
874
875
876
877
878 %plot times
879 T_forwardmodel
880 T_noisemodel
881 T_inversion
882
883 max(isnan(A),[],'All')
884 max(isnan(x_hat),[],'All')
885
886 % if print == true
887 %   addpath('/Users/z3bb0/Documents/GitHub/Retrieval-methods')
888 %   fid = fopen('/Users/z3bb0/Documents/GitHub/Retrieval-methods/test_data.txt↔
      ', 'w')
889 %
890 %   %print frequency
891 %   fprintf(fid, '%.2f \t', f*1E-9);
892 %   fprintf(fid, '\n');
893 %   fprintf(fid, '\n');
894 %
895 %   %Print range values
896 %   fprintf(fid, '%.2f \t', r);
897 %   fprintf(fid, '\n');
898 %   fprintf(fid, '\n');
899 %
900 %   %Print slow time values (this just prints the same data N_T times, but real
901 %   %data would be different ofcourse)
902 %   N_T = 10;
903 %   Fs_slowtime = 10;%1/(T_int + T_process + T_wait)...
904 %   T = (0:N_T-1)/Fs_slowtime;
905 %
906 %   fprintf(fid, '%.2f \t', T);
907 %   fprintf(fid, '\n');
```

```
908 %     fprintf(fid, '\n');
909 %
910 %
911 %     %Print Pr_matrix (linear)
912 %     for i = 1:N_T
913 %         for j = 1:N_r
914 %             fprintf(fid, '%.6E \t', Pr_matrix(j,:));
915 %             fprintf(fid, '\n');
916 %         end
917 %     end
918 %     fclose(fid);
919 % end
```

DEPARTMENT OF SOME SUBJECT OR TECHNOLOGY
CHALMERS UNIVERSITY OF TECHNOLOGY
Gothenburg, Sweden
www.chalmers.se



CHALMERS
UNIVERSITY OF TECHNOLOGY